Mechanical-Structural Investigation of Ion-Exchanged Lithium Silicate Glass using Micro-Raman Spectroscopy

Courtney Calahoo,[†] J. W. Zwanziger,[*,†] and Ian S. Butler[‡]

[†]*Department of Chemistry and Institute for Research in Materials, Dalhousie University, PO Box 15000, Halifax, NS B3H 4R2, Canada, and* [‡]*Department of Chemistry, McGill University, 801 Sherbrooke St. West, Montreal, QC H3A 0B8, Canada*

E-mail: jzwanzig@dal.ca

Phone: +1 902 494 1960. Fax: +1 902 494 1310

Abstract

Micro-Raman spectroscopy was used to determine the structural modifications occurring in a simple ion-exchanged glass. The base lithium silicate composition $30Li_2O$-$70SiO_2$ was studied as it underwent ion exchange, $Li^+ \leftrightarrow K^+$, at six temperatures spanning the glass transition point. Using a well-developed relationship between the Si-O-Si bond angle, Si-O bond length, and Raman shifts, the reduction in network molar volume and increase in compressive stress were estimated. Based on the effect of the ion exchange temperature, the existence of a threshold energy below which the compressive stress manifests as the re-orientation of silica tetrahedra only, and above which, the system relaxes by increasing the Si-O bond-length, is proposed. Finally,

*To whom correspondence should be addressed

[†]Dalhousie University

[‡]McGill University

the linear network dilation coefficient is revisited in terms of these new data, and an explanation given for its underestimation and overestimation of stress at low and high temperatures, respectively.

Introduction

The ion-exchange (IE) process enhances mechanical and optical properties, namely increasing strength up to 4-6 times, thereby broadening the scope of high-stress applications where glass can be used: hand-held media device screens, heat-resistant fireplace windows, waveguides, micro-optics, airplane cockpit and high-speed train windshields, drug-delivery equipment, and eye-glasses.[1–4] As glass is a brittle material, the reason for failure is rarely insufficient stiffness; the surface condition usually plays a larger role, where tiny flaws act as local tensile-stress concentrators and give rise to fracture. Ion-exchange offers a solution to this problem: it increases scratch-resistance by generating an opposing compressive stress at the surface. Uniquely, IE produces high stresses, several hundreds of MPa,[1,4–6] over a shallow case depth, ≤ 100 μm, which allows objects that cannot undergo thermal tempering, e.g., irregularly-shaped and thin glass objects, to be strengthened nevertheless. Due to the compositional gradient, birefringence can be used to produce waveguides and the resulting changes in refractive index have been measured optically;[3] nonetheless, the resulting stress profile is important as different stress states can affect the refractive index further.[7,8]

The IE process is performed by placing the target object in a molten salt bath, *e.g.,* KNO_3, and the exchange is driven by ion-concentration differences between the inside of the glass and salt bath. When performed below the glass transition temperature, T_g, IE induces compressive stress on the glass network due to a larger ion filling a cavity recently vacated by a smaller ion, while preventing significant relaxation or accommodation of the larger invading ion. Commercial IE glasses such as Corning Gorilla® and Schott Robax® have smaller ions, such as Na^+ or Li^+ ions, respectively, replaced with larger K^+ ions which can yield strength enhancements up to 2–4 times, improve hardness by 8–20% and decrease

fragment size substantially.[6,9] Additionally, the refractive index of the exchange-layer can be altered over a shallow depth by introducing an ion with a different polarizability.[4,10,11]

Many experimental studies use birefringence to probe directly the compressive stress found in the IE layer; stresses are typically on the order of hundreds of MPa up to 1 GPa spread over case depths of 20-1000 μm.[1,5,6,12,13] The duration of the IE treatment affects both the magnitude and location of the maximum compressive stress; the maximum stress has been shown to decrease and migrate further from the glass surface with increasing IE duration. The maximum induced stress occurs when IE is performed at temperatures well below the T_g, roughly 120–250 °C[5,12,13] below. Nonetheless, substantial compressive stress, approximately half of the maximum, has been observed even when IE took place only 30 °C below T_g, yet for the same amount of time as the maximum compressive stress.[5,14] Finally, even temperatures 135 °C below T_g have shown significant stress relaxation over a long enough period, 72-216 h,[1,5,12,13,15] highlighting the possibility that the glass network will relax under sufficient stress, despite being well below T_g. It is important to remember that T_g is a broad transition and that the viscosity of the material is still significant at these temperatures.

A recognized problem in IE glasses is the anomalous behaviour of the linear network dilation coefficient (LNDC), B, defined as the linear strain per unit change in alkali concentration, where V_m is the molar volume and C_{M^+} is the concentration of invading cation:[2,16–18]

$$B = \frac{1}{3}\left(\frac{1}{V_\mathrm{m}}\frac{\partial V_\mathrm{m}}{\partial C}\right) = \frac{1}{3}\frac{\partial \ln V_\mathrm{m}}{\partial C_{\mathrm{M}^+}}. \tag{1}$$

As the molar volume of the exchange layer of an IE glass cannot be measured directly, B for IE glasses is typically calculated from the optically measured stress, σ, using the following relation developed by Cooper and Krohn:[19]

$$\sigma(z) = -\frac{BY}{1-\nu}\left[C_{\mathrm{M}^+}(z) - C_\mathrm{avg}\right]. \tag{2}$$

It is dependent on Young's modulus (Y), Poisson's ratio (ν), stress as a function of distance from the IE surface (σ(z)), concentration of substituting ion, (C_{M^+}(z)) and average concentration of substituting ion ($C_{\mathrm{M}^+\mathrm{avg}}$). These last two terms enforce that the total stress in the glass, compressive and tensile, sum to zero. Additionally, if there is no concentration gradient, the stress is also zero. Conversely, V_{m} and the corresponding B, can be calculated from combined Metropolis Monte Carlo (MC) and molecular dynamics (MD) simulations.[16,20]

The observed anomalous behaviour comes about when B for IE glasses is compared to the corresponding as-melted mixed-alkali glasses; B is always 2–5 lower in IE glasses. B depends on the IE temperature, where the lowest B is typically found at processing temperatures of approximately $0.8T_{\mathrm{g}}$.[19,21] For example, an $\mathrm{Na}^+ \leftrightarrow \mathrm{K}^+$ exchange in a silicate glass has a measured LNDC of 3–5$\times10^{-4}$ (mol-% $\mathrm{K_2O}$)$^{-1}$ compared with a LNDC of 1.3$\times10^{-3}$ (mol-% $\mathrm{K_2O}$)$^{-1}$ for the as-melted series.[2] This order-of-magnitude discrepancy is likely because the molar volume of an IE-glass is less than the corresponding as-melted composition; models have shown that the local molar volume in an IE glass is approximately half of the as-melted composition and this has been used to calculate the experimentally-observed LNDC, about 2-4 lower than the bulk as-melted glasses.[16,17,20,22] Nonetheless, thus far, the molar volume of the exchange layer in an IE glass has not been measured experimentally, nor has any specific mechanism for stress generation or relaxation been reported, only mechanisms from simulations have been suggested. As the case depth is on the order of tens of microns, many typical analysis techniques are unsuited to examining the local structure of the IE layer, one exception being micro-Raman spectroscopy. This has the advantage that it can probe the molecular structure with < 1 μm lateral spatial resolution.Moreover, the energies of Raman vibrations can be related to external Si-O-Si bond-angles between $\mathrm{SiO_4}$ tetrahedra and internal Si-O bond-lengths within each tetrahedron;[23–27] thus, Raman spectroscopy offers a unique insight into the silica network structure.

It has been reported that if the exchange is done below T_{g}, the ion coordination number is similar to what is expected from the bulk as-melted composition.[16,17,28] However, there is

some disagreement as to whether the glass network connectivity, remains unaltered.[4,16,17,29] Investigations of IE glasses using micro-Raman[4,29] and X-ray absorption[28] spectroscopy have both observed changes in the topological structure. Furthermore, it has been proposed that changes in Q^n-populations could reduce the accumulation of compressive stress within the IE layer.[30] Kreski et al.[17] used simulations to show the topological structure of the IE glasses remains the same, *i.e.,* like the untreated material, yet they possess the local cation environment of the invading ion, thereby leading to constraints on the possible molar volume. On the other hand, a computational study by Tandia et al.[16] attributed the LDNC anomaly to differences in local cation site between as-melted and IE glasses. Unfortunately, Raman spectroscopy is incapable of measuring changes in the alkali environment, however, it can investigate how the connectivity of the glass network is affected by IE and IE temperature alike.

Computational studies[16,17] also discuss how the compressive stress and relaxation manifests structurally. Kreski et al.[17] attributed the residual strain in the system to an increase in cation coordination sphere, evidenced by oxygen atoms being pulled towards the alkali site and a re-orientation of SiO_4 tetrahedra, namely an *increase* in ∠Si-O-Si beyond what is found in the as-melted potassium end-member composition. Tandia et al.[16] describe the relaxation of the structure as a two step process: an initial fast rearrangement of the cation site towards a mixed-alkali as-melted structure indicated by an elastic expansion, followed by a slow process towards the as-melted potassium end-member structure manifested as an irrecoverable densification without network expansion. The first step is thought to induce the strain found in IE glasses, while the slow rate of the second step is responsible for the lower molar volume and LNDC anomaly seen in IE glasses. Another study corroborates these findings by explaining that the network is expanding elastically initially and then plastically contracting to relax stress.[31]

Several authors have attributed the anomalous behaviour of the LNDC to a slow plastic relaxation of the network.[15,30,32–34] Although the densification due to IE is thought to be

irreversible on the laboratory time scale, back-exchange simulations, where the invading ion is re-exchanged for the original ion type, showed the structural changes to be nearly completely reversible or elastic. Since this mechanism involves two different rate-steps, exchange and back-exchange, it may be more accurately described as non-linear elasticity.[16,17,20]

As ion-exchanged glass is used heavily in applications, it is important to fully understand the structural changes that lead to its enhanced mechanical properties. One of the major foci in this field is to improve further upon the enhancement, whether it is by using a specialized IE treatment or different materials. The goal of the present work is to explain the structural mechanisms which result in compressive stress in hopes of providing insight into improving the IE process. In this study, we determine the effect of ion exchange treatment temperature on structural modifications in IE glass using Raman spectroscopy. We also investigate the structural mechanisms that lead to compression within the silica network, and the type of mechanical behaviour they exhibit.

In this study, a simple binary lithium silicate, $30Li_2O$-$70SiO_2$ was used as the base glass. The samples were thermally ion-exchanged in KNO_3, $Li^+ \leftrightarrow K^+$, at six different temperatures between 360–480 °C, spanning the glass transition temperature, for 72 hours each. Micro-Raman spectroscopy and Wavelength Dispersive Spectroscopy (WDS) were used to examine the structure and composition, respectively, in order to address the issues mentioned above. This system was chosen for three reasons: simplicity of composition in comparison to many commercially-available IE glasses;[4] technological relevance, (Schott's Robax® is a commercially-available IE glass that involves Li^+-for-K^+); and amenability to analysis, as the Raman spectra show significant differences between glasses in the lithium and potassium disilicate region.[23–25]

Experimental

Glass preparation

The base glass, $30Li_2O$-$70SiO_2$, was prepared using Li_2CO_3 ($\geq$ 99%, Sigma-Aldrich) and SiO_2 (purum p.a., Sigma-Aldrich) by the conventional melt-quench method, melting at 1550 °C in a Pt crucible for 2 hours, quenching in air, followed by annealing at 415 °C overnight. Additionally, the bulk as-melted xLi_2O-$(30-x)K_2O$-$70SiO_2$ series was made for comparison, using a similar procedure, except annealing between 415–450 °C overnight and using dried (400 °C, 2 hrs), granular K_2CO_3 ($\geq$ 99%, ACP) as a starting material. Samples with large amounts of K_2CO_3 were seen to bubble rapidly at $\approx$ 800 °C, as supported by K_2CO_3 having a decomposition temperature of $\geq$900 °C;[35] thus, small batch sizes, 7g, were used. Homogeneity and complete relaxation were confirmed optically using crossed polarizers to detect residual strain. Additionally, T_g measurements were made on the $30Li_2O$-$70SiO_2$ and $20Li_2O$-$10K_2O$-$70SiO_2$ bulk glasses using differential scanning calorimetry with a heating rate of 10 °C in an Ar environment. The Netzsch DSC 404 F1 Pegasus instrument has a precision of $\pm$ 2 °C.

Ion-exchange Procedure

A large piece of base glass was cut into several smaller pieces, approximately $1 \times 1.5 \times 0.5$ cm; each piece was ion-exchanged in a fresh bath of KNO_3 ($\geq$ 99%, APS) in an N_2 atmosphere. The N_2 was used to prevent the oxidation of the nitrate to the carbonate or oxide form which was seen to occur in a similar experiment involving $Ca(NO_3)_2$. Six samples were ion-exchanged for 72 hours, each at a different temperature between 360–480 °C; the conditions include temperatures both below and above the glass transition temperature, T_g, of this glass composition (measured to be 459 °C). An IE processing time of 72 hours was chosen because soda-lime glass exchanged at that time scale showed significant and differing case depths for a range of IE temperatures.[1] After 72 hours, the samples were removed from the oven;

examination of the specimens through crossed polarizers revealed no significant additional residual strain generated by this procedure. The mass of the samples was measured before and after the exchange treatment. Once the samples had been washed with water and thoroughly dried, they were placed in epoxy to obtain an epoxy disc. The discs were then roughly polished with 30 μm diamond paper until the epoxy and glass surface were flush, whereby the top IE layer was mechanically removed and the compositional profile exposed. The exposed surface was then polished down to 1 μm, as shown in Fig. 1a). Case depth is defined, per metallurgy, as the thickness of the hardened layer of a specimen; it increases with distance away from the IE surface or specimen edge as shown in Fig. 1b).

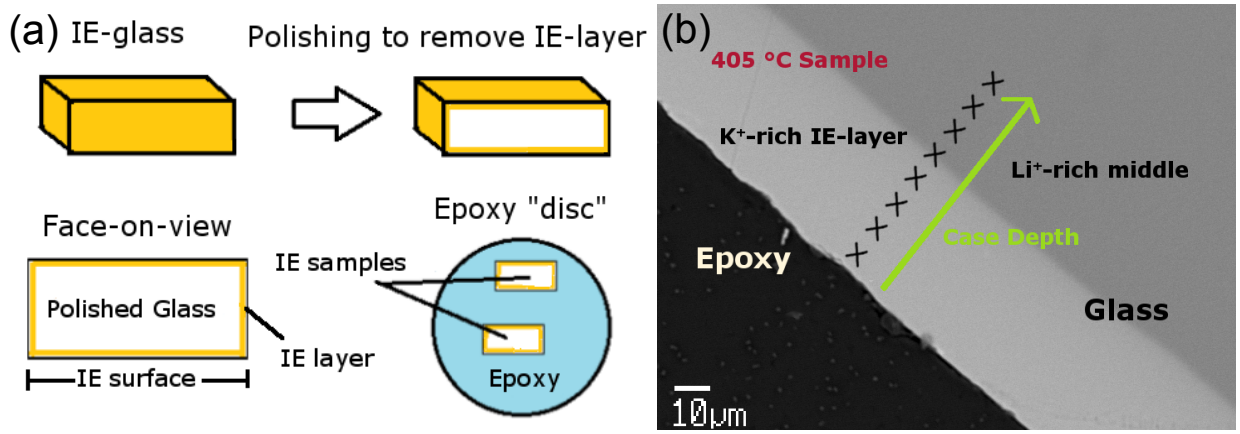

Figure 1: (a) Procedure for IE layer exposure and epoxy "disc" preparation for analyses. (b) Example of procedure for both WDS and Raman analyses, showing the case depth. The K^+-rich region appears lighter in colour.

Elemental Analysis

The compositions of the as-melted series were confirmed by inductively coupled plasma optical emission spectrometry (ICP-OES) with the exception of $30Li_2O$-$70SiO_2$, which was measured by wave dispersive spectroscopy (WDS) using a JEOL 8200 Superprobe. Since WDS has a spatial resolution of 1-2 μm, it was also used to confirm the IE process and create a quantitative composition profile. WDS is incapable of measuring any elements lighter than boron, thus, lithium content was not measured directly, but calculated from

the oxygen, silicon and potassium content and assuming correct stoichiometry. Sanidine was used as the standard in WDS to accurately determine K, Si and O concentrations, with errors depending on the element mass-%; for elements ≥ 2 mass-%, error is 0.3 mass-%, while elements < 2 mass-% have errors of 0.2 mass-%. Quantitative point analysis was performed at approximately nine μm intervals from the IE surface (with the exception of the 390 °C sample, which had approximately seven μm intervals), as calculated from the XYZ stage data of the WDS instrument; an example is illustrated in Fig. 1b), where $\times$'s represent points of composition analyses. The translation of the WDS stage is accurate to $\pm$ 1 μm. Finally, more qualitative line profiles were also collected across these samples using WDS.

Raman Spectroscopy

Raman spectra were collected using a Renishaw inVia micro-Raman spectrometer with a 514.5 nm argon-ion laser for 12 scans of 10 s each with a resolution of 1 cm^{-1}. The laser spot size was approximately five microns in diameter. The composition profile was conducted as follows: the first point was as close to the interface between the epoxy and the glass as possible without obtaining a large fluorescence signal observed when the epoxy was excited by the laser. We estimate this to be approximately six microns from the edge. Afterwards, the focal point of the laser was translated inward between 10-100 mum (smaller steps within the IE layer, larger past the layer); the step distance was determined by the scale on the eyepiece of the microscope and instrument viewing screen. Some distinct features were noted on the sample surface and the sample stage was moved accordingly, as a result the error is estimated to be roughly $\pm$ 1 μm. The procedure is similar to the one for the WDS point analyses, thus, Fig. 1b) applies again, where $\times$'s represent points of Raman analyses. Baseline correction and peak deconvolution were done using the Wire software program from Renishaw.

Results

Elemental Analysis

The analyzed compositions for the as-melted mixed alkali series are presented in Table 1. Although lithium was only measured indirectly for the $30Li_2O$-$70SiO_2$ sample, the elemental analysis from WDS is consistent with the nominal composition.

Table 1: Verification of glass composition from ICP-OES and WDS

Nominal Composition	Actual Composition		
	Li_2O	K_2O	SiO_2
$30Li_2O$-$70SiO_2$ [a]	31.4	0.4	68.5
$20Li_2O$-$10K_2O$-$70SiO_2$	19.4	11.8	68.4
$15Li_2O$-$15K_2O$-$70SiO_2$	14.5	15.1	70.1
$30K_2O$-$70SiO_2$	0.0	27.9	70.9

[a] Calculated from WDS results

Fig. 2 shows the K_2O mol-fraction in the IE glasses as a function of case depth (defined as IE layer thickness) as measured by WDS; the complete elemental analysis results can be found in the Supplementary Information. The WDS results show the highest K_2O content found in the IE glasses to be 9.3–9.5% (for only two points sampled by WDS), while 8.0–8.5% is the common K_2O content near the IE surface. The maxima near the surface in the 405 and especially the 420 °C sample are not expected from diffusion theory,[40] unless large amounts of Li^+ are transferring from the glass to the salt bath, and are likely an artefact of the surface condition. A mole fraction of 0.085 for K_2O corresponds to a relative Li_2O fraction of 0.72, therefore all the IE-glass compositions are in the range of 0.72–1 Li_2O total alkali fraction.

Raman Spectra

Micro-Raman spectra collected at increasing depths from the IE surface are shown in Fig. 3a–g) for different conditions: untreated (no IE) and six different treatment temperatures between 360–480 °C. For comparison, Fig. 3h) presents the Raman spectra of the mixed-alkali

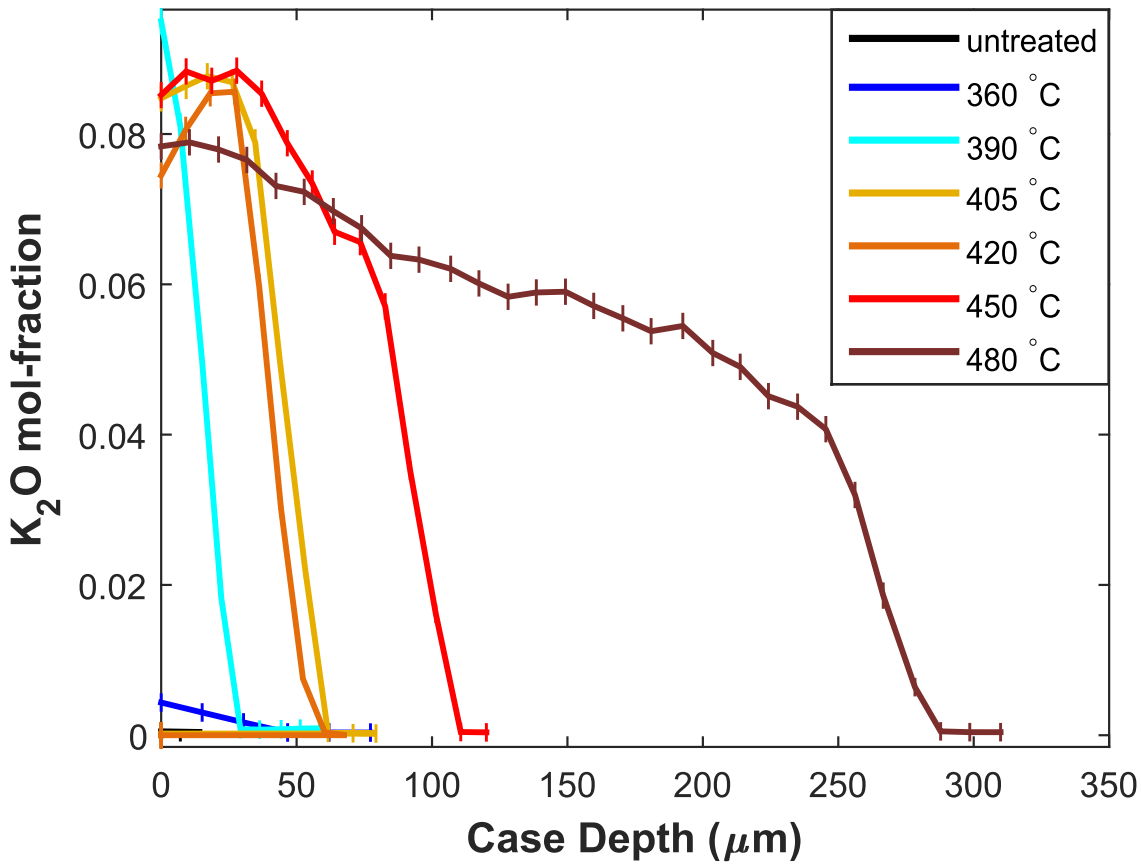

Figure 2: K_2O mol-fraction of IE glasses as a function of distance from the IE surface or edge, determined by Wavelength-Dispersive Spectroscopy (WDS). Error estimates depend on the mass of the analyte, which can be converted to mol-fraction for this glass system. When K_2O has a mol-fraction ≥ 0.01, the error is 1.0–1.6×10^{-3} mol-fraction, while for a mol-fraction < 0.01, the error is 0.4×10^{-3} mol-fraction.

as-melted bulk series, xLi_2O-$(30-x)K_2O$-$70SiO_2$. The effect of the invading K^+ ions on the glass structure is noticeable in temperatures at and above 390 °C. Most clearly, the high-frequency (HF) region peaks (900–1200 cm^{-1}) shift to higher wavenumbers and the low-frequency (LF) peak at approximately 480 cm^{-1}) decreases in intensity as K_2O content increases near the edge of the sample. Comparing these observations to the as-melted series in Fig. 3h), the trends are similar as the series goes from lower to higher K_2O content, with the exception of the narrowing of the major band in the LF-region.

Fig. 4a) compares the Raman spectra collected past the IE layer into the untreated portion of the sample, indicating samples were mostly unaffected by the ion-exchange process past the case depth, when the temperature was far enough below T_g, 459°C. However, the 450 and 480 °C samples did show some differences in the Raman spectra past the case depth. On the other hand, the comparison of the Raman spectra at the edge of each sample, Fig. 4b), shows the temperature-dependence of the IE process.

Discussion

Raman Shift Assignments

Silicate glass structure is often described in terms of Q^n-units, where n refers to the number of bridging oxide (BO) bonds, i.e., Si-O-Si bonds, found around a tetrahedral SiO_4-unit. The three low-frequency (LF) region Raman peaks at approximately 480, 570 and 630 cm^{-1} have been assigned to symmetric Si-O-Si stretching plus bending of Q^4, Q^3 and Q^2-units, respectively.[24,25] These vibrations are thought to be somewhat dependent on long-range interactions, in addition to being dependent on the external Si-O-Si bond angle, where a shift to higher wavenumbers indicates a reduction in angle.[24–26] Within the alkali and alkali-earth silicates, only K_2O-SiO_2 was seen to have easily resolved 570 and 630 cm^{-1} bands.[24] In the mid-frequency region, there is a single peak between 790–800 cm^{-1}, identified as a highly depolarized or antisymmetric Si-motion in a cage;[24] it has been observed to shift to

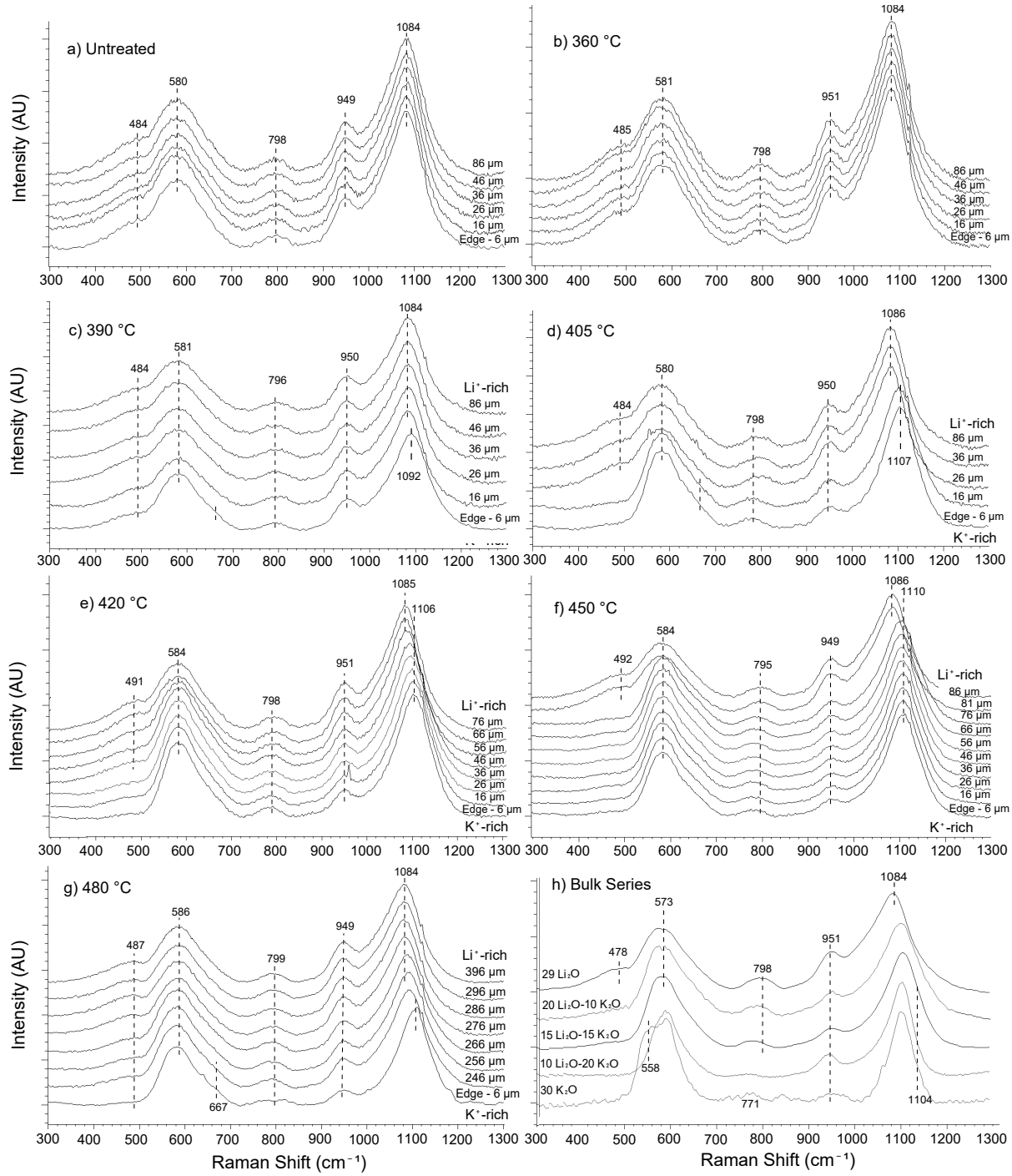

Figure 3: Micro-Raman spectra of the IE glasses treated at different temperatures at increasing depths from the glass surface: (a)untreated (b)360 °C (c)390 °C (d)405 °C (e)420 °C (f)450 °C and (g)480 °C. Where IE has occurred, the edge of the glass is relatively K^+-rich compared to deeper into the specimen, which closely matches the spectra of the untreated parent glass shown in (a). The error in the stage movement, corresponding to increasing case depth is ± 1 μm. The Raman spectra of the as-melted mixed-alkali xLi_2O-$(1–x)K_2O$-70SiO2 series as a function of composition are shown in (f).

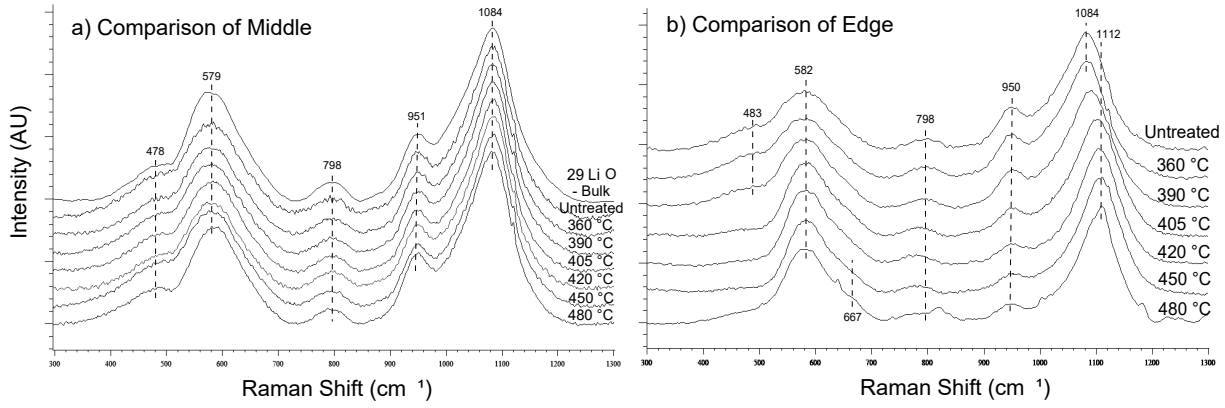

Figure 4: (a)Comparison of micro-Raman spectra collected far from the edge of each IE specimen, 360 °C–480 °C and untreated, with as-melted $30Li_2$–$70SiO_2$, indicating the effect of the IE process is negligible past the IE layer. (b)Comparison of micro-Raman spectra collected at the edge (highest K^+ conc.) of each IE specimen, 360 °C–480 °C and untreated, showing the effect of heat and K^+-concentration.

lower wavenumber with increased alkali content.

Peaks in the high frequency (HF) region are due to localized Si-O stretches within the silicate tetrahedra; as a result peaks in the HF-region can be used for quantification of Q^n-species in the glass structure. In the case of the HF bands, the Raman shift is a function of internal Si-O bond-length, where with the exception of Q^4-units, a higher wavenumber corresponds to a shorter Si-O bond. The three peaks in the HF-region at approximately 945, 1040, 1090 and 1120 cm^{-1} were assigned to symmetric Si-O^- stretches of Q^2, Q^4, Q^3 and $Q^{3'}$-units, respectively (that is, Q^3 with two different second-neighbour environments).[23–25]

There is some disagreement in the literature about the assignment of the HF shoulder at $\approx$ 1120 cm^{-1} ($Q^{3'}$ vs. $Q^{4'}$ [25,41,42]). Matson et al. observed the $\approx$ 1150 cm^{-1} shoulder in high-alkali silicates and assigned it as a distinct $Q^{3'}$-species due to its having the same polarization ratio as the main Q^3 peak, its merging with the main Q^3 peak at the disilicate region and the fact that its intensity does not correlate with the intensity of the known LF Q^4 peak at $\approx$ 480 cm^{-1}. As the near-disilicate composition used here, $30Li_2O$-$70SiO_2$, is known to be mostly composed of Q^3-units and the Raman peak intensity of shoulder at 1115 cm^{-1} was actually found to correlate *negatively* with the LF Q^4 peak at $\approx$ 480 cm^{-1},

the shoulder was assigned as $Q^{3'}$. Compared to other alkalis, Li_2O-SiO_2 has been found to possess a structure more similar to pure silica even at high modifier concentrations; their spectra retain the LF Q^4 peak (480 cm^{-1}) longer and the HF Q^n peaks have more equal Raman scattering efficiencies.[25] The Raman shift assignments are summarized in Table 2.

Table 2: Raman shifts (ν) and assignments for fitted peaks

Wavenumber (cm^{-1})	Vibrational Mode	Q-species
460–480	$(Si\text{-}O\text{-}Si)_s$ stretch	Q^4
560–580	$(Si\text{-}O\text{-}Si)_s$ stretch	Q^3
605–650	$(Si\text{-}O\text{-}Si)_s$stretch	Q^2
780–795	antisymmetric Si-motions in cage	
945–950	(O-Si-O) stretch	Q^2
1030–1070	$(O\text{-}Si\text{-}O)_s$ stretch	Q^4
1085–1110	$(O\text{-}Si\text{-}O)_s$ stretch	Q^3
1115–1160	$(O\text{-}Si\text{-}O)_s$ stretch	$Q^{3'}$ [a] or $Q^{4'}$ [b]

[a]From ref 25 [b]From ref 41

Fitting and Error Analysis

The fits for the middle of the untreated specimen and the edge of the 450 °C sample are shown in Fig. 5. It was challenging to fit the IE spectra due to the compositional gradient, nonetheless, eight peaks were found to fit all the spectra reasonably well, with a maximum $\chi^2 \leq 12$, while still having valid peak assignments. No restrictions were placed on the fits other than using pure Gaussian lineshapes[24] and limiting the possible peak width of the HF-region peaks to ≤ 100 cm^{-1}, which is supported by literature peak bandwidths.[24,41]

The errors for these fits in peak area and position, are standard errors calculated at the 95% confidence level using the spectra from the compositional plateau found past the IE layer. As Raman spectra were collected beyond where K^+ was able to diffuse into the glass structure, there is a plateau in the fitted peak values, where the Raman spectra are essentially replicates of the untreated glass, $30Li_2O$-$70SiO_2$, collected from different spots along the surface. These errors are then applied to the entire sample, including the mixed-alkali gradient region near the edge. As each IE temperature has a plateau past the case

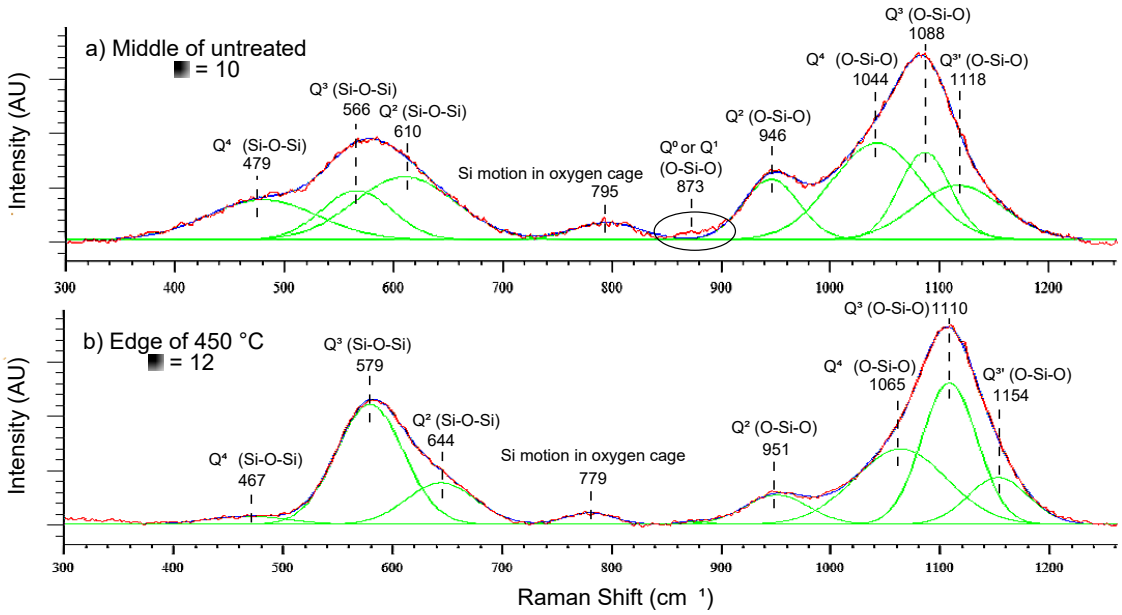

Figure 5: Peak deconvolution for two samples: (a) middle of untreated parent glass, $30Li_2O$-$70SiO_2$ and (b) edge (highest K^+ conc.) of IE glass at 450 °C treatment. Lines are only guides for the eyes.

depth, there is a unique error corresponding to that sample. Overall, this strategy appears reasonable as most of the error is due to the fitting procedure rather than the data collection. In the case of the 480 °C sample, the compositional plateau near the edge was used instead of the pristine plateau nearer the middle; this larger variance in composition may be responsible for some of the larger errors seen for 480 °C in Fig. 8a).

Area Fraction

Although Raman spectroscopy is not a quantitative analysis technique, it is possible to compare relative peak areas within a spectrum. The spectra of the IE samples were collected consecutively, one point after another along the surface, maintaining experimental parameters for each sample. The Q^n distributions determined from the relative area of the four localized HF-region peaks are shown in Fig. 6. In this case, the Q^3 and $Q^{3'}$-units were grouped together, to make the graphs clearer and easier to compare to literature. The errors were tabulated from the plateau spectra of the middle region of each sample as explained in

the previous section. As the Q^3 fraction is actually composed of two peaks, Q^3 and $Q^{3'}$, it generally has twice the error of the other two Q^n-units in Fig. 6. In the case of the as-melted mixed-alkali series, Fig. 6h), the errors were simply taken to be $\pm 10\%$ of the area fraction per literature procedures.[41] It is encouraging that although the errors for the IE glasses and the as-melted series were determined by different routes, they are comparable.

For exchange temperatures ≥ 390 °C, a clear effect of the invading K^+-ions is observed: at the edge of the ion-exchange glass, where there is the highest concentration of K^+-ions, there is a higher area-fraction of Q^3-species, 0.55, in comparison to the middle of the glass, 0.45. Along with the decrease in Q^3-species, there is a concurrent increase in Q^2 and Q^4-species towards the middle of the sample. This trend is similar to the disproportionation reaction, $2Q^3 \leftrightarrow Q^2 + Q^4$, that is known to occur in bulk glasses.[25,43] The area-fraction of ion-exchanged glasses can also be compared directly to the as-melted mixed-alkali glasses shown in Fig. 6h). There is a slight increase in Q^3-species compared to what is expected from the corresponding as-melted compositions; this indicates that the IE glass Q^n populations exceed those in the corresponding as-melted mixed-alkali compositions and more similar to as-melted compositions with greater concentrations of K^+.

As the Raman cross-section is a result of changes in polarizability, and Q^n-units differ in charge and volume, they also differ in cross-section.[27,44,45] There is even evidence to suggest that the identity of the cation in a NBO can affect the strength of the Raman effect, although that is likely a minor contribution in comparison to the type of Q^n-species.[46] Nevertheless, the normalized cross-section, which relates the intensity of a Raman-active mode to its population, for a given Q^n-species can be determined empirically from known compositions and assumed to be roughly constant across a glass series.[27] Using the expected Q^n-population[47] for a glass with the untreated composition, $30Li_2O$-$70SiO_2$, and the spectral area of the assigned Raman peaks, normalized cross-sections were determined for each Q^n-species in the untreated sample ($Q^4 = 1.44$, $Q^3 = 0.70$ and $Q^2 = 1.50$); it was then applied to the corresponding peak area in the IE samples to produce a normalized Q^n-population,

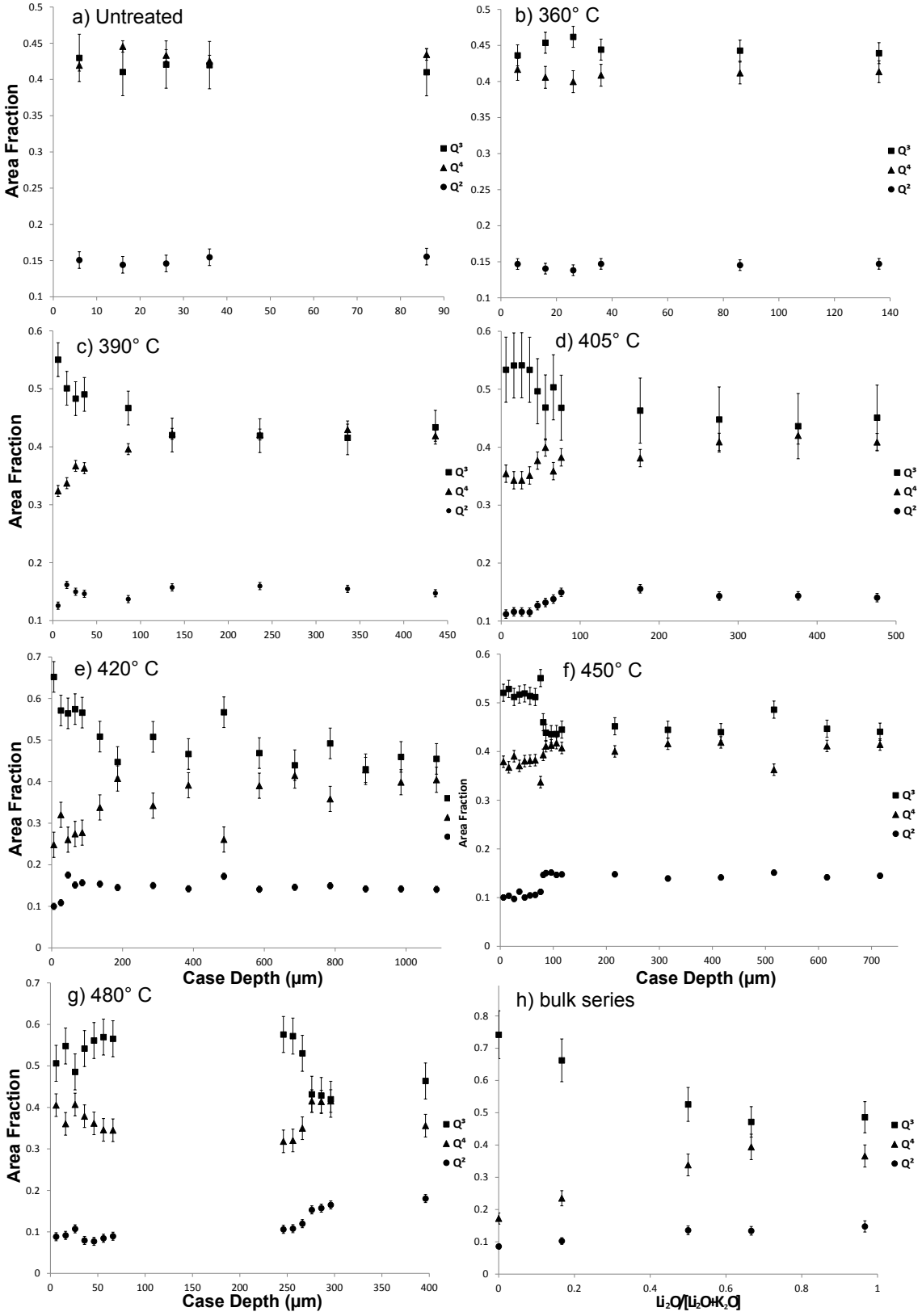

Figure 6: Normalized area of the HF-region Raman Peaks corresponding to Q^2(♦), Q^3(■), and Q^4-unit(▲) fractions for all IE temperatures, untreated and 360–480 °C (a–g) as a function of case depth from the IE surface in comparison with the Q^n-fractions of the bulk, xLi_2O-$(30-x)K_2O$-$70SiO_2$ series in (h).

which will be used in the rest of the paper. Additionally, the structural changes are expected to be small in an IE glass, further validating the application of the normalized cross-sections estimated from the untreated sample to the IE spectra.

Non-Bridging Oxygens per Silicon Atom

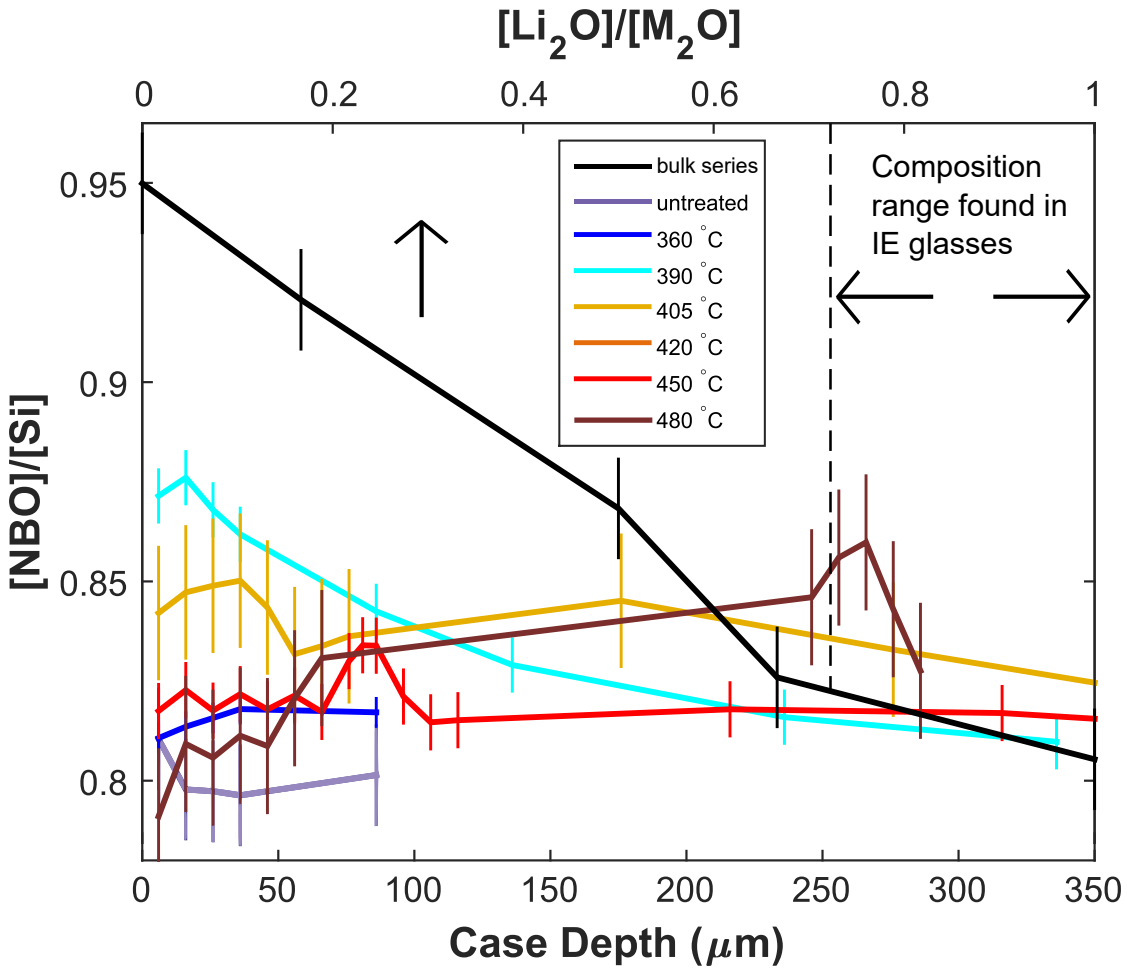

Figure 7: Connectivity, or non-bridging oxygen per silicon atom, [NBO]/[Si], for ion-exchanged glasses, untreated (purple) and 360–480 °C (dark blue–red), as a function of depth from IE surface (bottom axis) in comparison with [NBO]/[Si] in the bulk series (black) as a function of composition (top axis). All [NBO]/[Si], including the as-melted series, were determined from Raman spectroscopy and the calculated normalized cross-sections. For comparison, the range of $[Li_2O]/[M_2O]$ found in the IE glasses is also marked.

Using the normalized Q^n-distribution, the non-bridging oxygens per silicon atom $\big([NBO]/[Si]\big)$

of the different IE-samples can be calculated, as shown in Fig. 7. The [NBO]/[Si] ratio gives a more comprehensive picture of what is occurring in the glass structure compared to the Q^n populations alone. Fig. 7 also includes the [NBO]/[Si] ratio of the as-melted mixed-alkali series (plotted against composition along the top axis) for comparison, which match the [NBO]/[Si] determined from composition in Table 1 quite well. Fig. 7 indicates that as-melted glasses with similar compositions to that of the IE layer ($[Li_2O]/[Li_2O+K_2O]$ of 0.72–1) would have [NBO]/[Si] of 0.8–0.82. Samples treated at higher temperature, 450 and 480 °C, have an [NBO]/[Si] ratio of approximately 0.81 near the outer edge, which is fairly close to what was found for the compositionally equivalent as-melted glass, 0.82. Both of these temperatures are near enough to T_g to relax the structure towards that of the as-melted sample. However, the 480 °C sample shows a steady increase in [NBO]/[Si] from 0.81 to 0.87 with increasing case depth until decreasing sharply near the transition from IE layer to pristine composition. Additionally, for the samples treated at lower temperature (390–420 °C) the [NBO]/[Si] ratio is higher, especially near the outer edge, than what was found for the corresponding as-melted mixed-alkali composition. Consequently, this increased [NBO]/[Si] may be a feature found within all unrelaxed IE layers. This result indicates a *reduction* in connectivity, which is the opposite of what is normally associated with enhanced mechanical properties. These larger than expected ratios indicate a modification in how the charge balance of the glass is being maintained; there are Si-O-Si bonds being converted into $Si\text{-}O^-M^+$, perhaps simply to accommodate the substituting K^+-ion which has twice the desired oxygen coordination number of Li^+ (8 vs. 4).[48] Computational studies have showed the invading cation oxygen coordination to be somewhere between what is found in the untreated and as-melted compositions.[16]

Additionally, the WDS results (presented in SI) show less SiO_2 content within the IE layer in comparison to the middle of the sample, which may be due to larger ions blocking ion channels, preventing the smaller ions from leaving, creating a build-up of "extra" ions leading to more NBOs. In any case, the peak area data show clear evidence for structural

rearrangement, *i. e.,* breaking and forming bonds, becoming more similar to the as-melted mixed-alkali structure and is supported by other experimental literature.[4,29] Nonetheless, the differences in connectivity between the IE layer and as-melted mixed-alkali series is likely not responsible for the improved mechanical properties seen in IE glasses.

Shifted Raman Shifts

For our purposes, a more useful way to represent the peak positions is the shift of the Raman shift, $\Delta\nu$, defined as the difference between the Raman shift of a peak in a sample, ν_{s} and the shift of the corresponding peak of the untreated or the endpoint composition of the as-melted series, $30Li_2O$-$70SiO_2$, $\nu_{30\mathrm{Li_2O}}$.

$$\Delta\nu = \nu_{\mathrm{s}} - \nu_{30\mathrm{Li_2O}} \tag{3}$$

$\Delta\nu$ is a quantifiable measure of the any structural changes caused by the replacement of the Li^+ with K^+ ions in the IE samples. It was determined at each depth from the IE surface for all eight major peaks identified from fitting, Fig. 8 and Fig. 9. The three LF-peaks at 480, 560 and 610 cm^{-1} presented in Fig. 8a-c) are assigned to symmetric Q^4, Q^3 and Q^2 Si-O-Si stretches, respectively, and have been correlated to the external Si-O-Si angle.[23–27] The plots in Fig. 9a–d) show the $\Delta\nu$ of the four peaks in the HF-region, 945, 1040, 1090 and 1125 cm^{-1}. As stated earlier, the positions of these peaks are correlated with the Si-O bond-length of the structural Q^n-units found in the glass. The errors were calculated for each temperature using the method described in the previous *Fitting and Error Analysis* section. Typically, the error was on the order of $\pm$0.5–2.5 cm^{-1}, with the outer, 480 and 1120 cm^{-1}, and weaker, 795 cm^{-1}, peak fits having the largest variance.

Raman shifts for the as-melted mixed-alkali series can be found in the SI. The $\Delta\nu$ for the as-melted composition which corresponds to the highest K^+ composition found in the IE glasses (approximately $21Li_2O$-$9K_2O$-$70SiO_2$) is tabulated in Table 3. The error in the

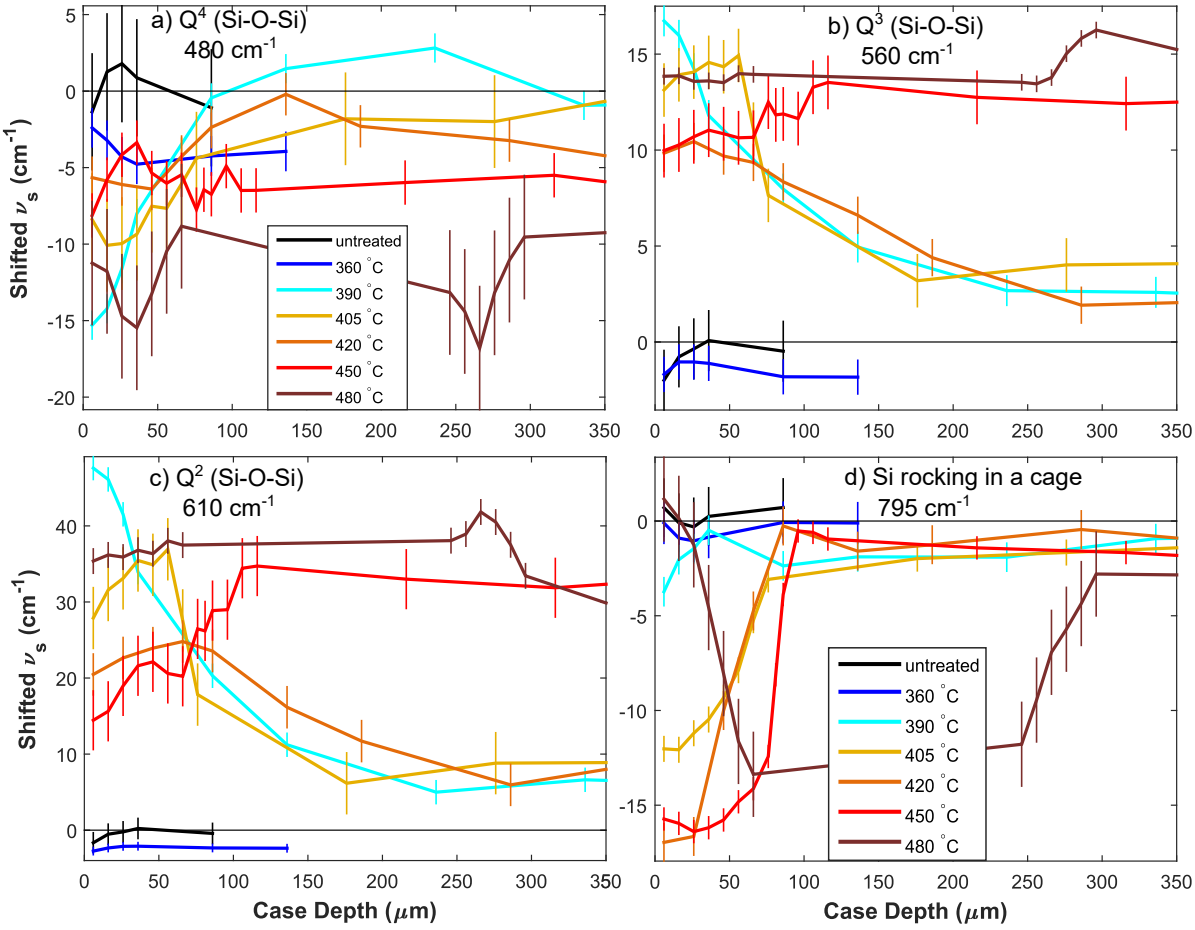

Figure 8: Shifted Raman shifts ($\Delta\nu$) for the low frequency Raman modes. $\Delta\nu$ is the difference between the Raman shift in the IE layer and the untreated parent glass for a given mode, plotted here as a function of ion-exchange depth for all IE-temperatures. Colors: untreated (black) and 360–480 °C (purple–red). The positions of the first three Raman peaks in the LF-region are known to correlate with Si-O-Si bond angle in Q^n-species: (a)480 cm^{-1} Q^4, (b)560 cm^{-1} Q^3, (c)610 cm^{-1} Q^2, while the fourth peak is attributed to Si-rocking in a cage (d)795 cm^{-1}.

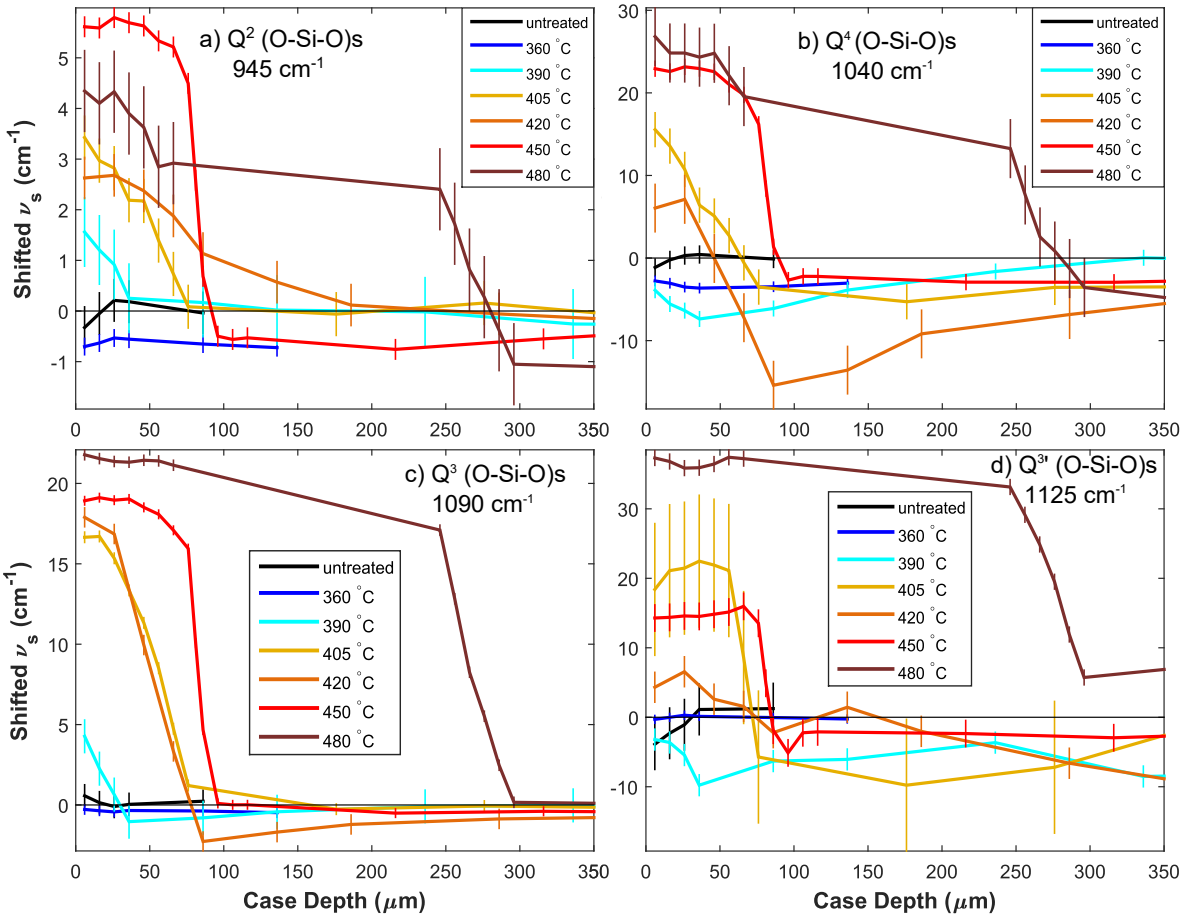

Figure 9: As in Fig. 8 but for the high freqency Raman modes. The positions of the four Raman peaks in the HF-region are known to correlate with Si-O bond-length in Q^n-species: (a)945 cm^{-1} Q^2, (b)1040 cm^{-1} Q^4, (c)1090 cm^{-1} Q^3 and (d)1125 cm^{-1} $Q^{3'}$.

as-melted $\Delta\nu$ is the average error found for each peak in the ion-exchanged samples.

Table 3: Shifted Raman shifts, $\Delta\nu$, for the as-melted mixed-alkali silicate with the same composition as the edge of the IE-samples, $\approx 21Li_2O\text{-}9K_2O\text{-}70SiO_2$.

Shift Range (cm^{-1})	Q^n-species	ν_c (cm^{-1})	Error (cm^{-1})
460-480	Q^4	-10	2.6
560-580	Q^3	3	1.1
605-650	Q^2	3	2.5
780-795	Si motions in cage	-8	1.2
945-950	Q^2	2.5	0.5
1030-1070	Q^4	15	1.7
1085-1110	Q^3	10.5	0.5
1115-1160	$Q^{3'}$	8	2.9

First of all, in Figs. 8 and 9, the shift $\Delta\nu$ is generally farther from the baseline, i.e., the untreated glass, for the samples treated at the highest temperatures. Beginning with Fig. 8a) (the 480 cm^{-1} peak), we see that this fit is noisier than the rest, but we can say with certainty that the low and high temperatures, 390, 450 and 480 °C, are shifting to lower wavenumbers than expected from the equivalent untreated composition. In contrast, the other two LF-region peaks, 560 and 610 cm^{-1} (Fig. 8b) and c)), have much larger increases in $\Delta\nu$, 7–16 and 12–45 cm^{-1} respectively, for all temperatures, compared with the untreated $\Delta\nu$, only 3 cm^{-1}, for both bands. Fig. 8d) shows that the negative $\Delta\nu$ value indicates replacing Li^+ with K^+ reduces the frequency of the Q^4-motion in a cage. Once more, the higher temperature samples, 405–480 °C have a larger deviation from the untreated sample of the same composition. Fig. 9 shows the higher temperatures, 420–480 °C, to have larger $\Delta\nu$ in comparison to the untreated composition. Overall, a larger deviation from the potassium-free composition is seen in the IE-samples, especially for the high-temperature conditions, in comparison to the equivalent untreated composition.

Raman-Crystal Calibrations

The Raman peaks of the IE glasses can be compared to those found in crystals of similar composition to understand how much the external Si-O-Si angles are changing. A calibration

curve of Si-O-Si bond angle vs. Raman shift was made using literature crystal data (Fig. 10). It was found that although a reliable trend ($R^2 = 0.88$) exists for alkali silicate crystals, where a higher wavenumber indicates a smaller Si-O-Si angle, there is no relation between Si-O-Si bond angle and Raman shift in SiO_2 polymorphs. This may be due to a lack of steric constraints in SiO_2 structures, where calculations have shown the energy per molecule in fused quartz varies only by 0.2 eV for a range of 120° to 180°.[49–51] As a result, little can be said about the ∠Si-O-Si of Q^4-units, consequently, an average ∠Si-O-Si (149°) is assumed for *all* IE and as-melted glasses alike. Additionally, the Raman peak position correlated with ∠Si-O-Si of Q^4-units, Fig. 8a), changes less than the other Q^n-unit peaks, Fig. 8b-c).

Alkali silicate crystals, on the other hand, appear to have more constraints and fewer possible crystal structures, for example, lithium and sodium silicates are iso-structural. Nonetheless, the relationship between Si-O-Si bond-angle and Raman shift in alkali-silicate crystals can be used to convert the shifted Raman shift, $\Delta\nu$, into an estimate of Si-O-Si bond-angle modification induced by the IE process. For example, the LF-region Q^2 and Q^3 Raman peaks positions increase by 35 and 14 cm^{-1}, respectively, at the surface of the 480 °C sample, which corresponds to a decrease of −7° (−5%) and −3° (−2%) in the Si-O-Si bond-angle. In the case of an IE temperature of 390°C, a $\Delta\nu$ of 48 and 17 cm^{-1} were observed, indicating a bond angle decrease of −9° (−7%) and −3° (−2%) for Q^2 and Q^3-units, respectively. This indicates that the Si-O-Si bond-angles of Q^2-units are more affected by the IE-temperature in comparison to Q^3-units, which is also observed in $\Delta\nu$, Fig. 8.

Like the LF-region peaks, the HF-region Raman peaks can be compared to crystal data to determine the approximate conversion between wavenumber and bond-length, Fig. 11. However, unlike Fig. 10, SiO_2 polymorphs have a stronger correlation between Si-O bond-length and Raman shift, $R^2 = 0.83$, while alkali silicates show a weaker trend between Si-O bond-length and Raman shift, $R^2 = 0.63$. It is interesting to note the trends are opposite for SiO_2 polymorphs compared to alkali silicates; although a negative relationship between bond-length and Raman shift is commonly seen, the opposite relationship observed

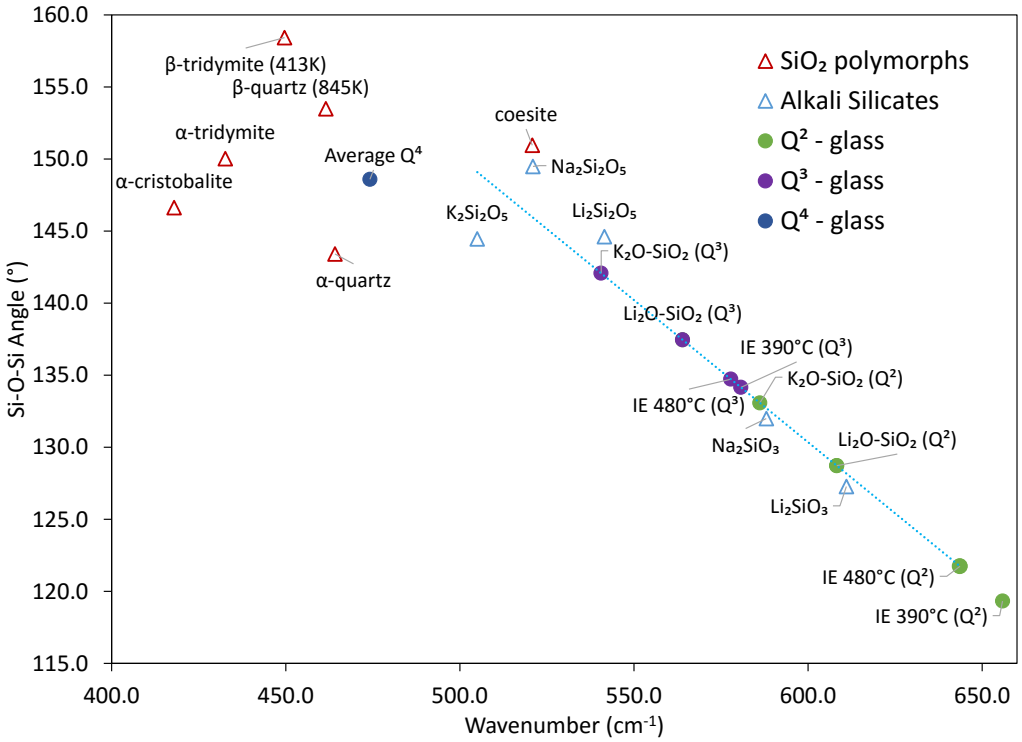

Figure 10: Calibration curve comparing average Si-O-Si bond-angle in crystal structures from literature to literature Raman data. Na_2SiO_3;[23,54–56] Li_2SiO_3;[23,56–60] $K_2Si_2O_5$;[23,61] $Na_2Si_2O_5$;[23,62,63] $Li_2Si_2O_5$;[23,60,64,65] coesite;[66–70] α-quartz;[69–86] α-cristobalite;[87–92] β-cristobalite;[89,91–94] α-tridymite;[95–97] β-quartz;[72,73,81,82,98–100] β-tridymite.[96,97,101] Literature values are available in the SI. SiO_2 polymorph crystals (△) do not have a correlation between Si-O-Si bond-angle and Raman shift, therefore, an average ∠Si-O-Si is suggested for the Q^4-units(●) in Li_2O-SiO_2, K_2O-SiO_2 and IE glasses based on the average measured Raman shift. The alkali silicate crystals (△) line-of-best-fit, $R^2 = 0.87$, was used to calculate the corresponding Si-O-Si bond-angles for the Q^2(●) and Q^3-units(●) in the Li_2O-SiO_2, K_2O-SiO_2 and IE glasses from the measured Raman shift. Errors in ∠Si-O-Si determined from the fit are ±4° (±3%) for both Q^2 and Q^3-units. For the Raman and crystal data, at least two separate literature values were averaged; however, for α and β-tridymite has one experimental and one calculated value.[97] Additionally, the crystal data only contains one value for the structures of $K_2Si_2O_5$ and $Na_2Si_2O_5$. As of now, the crystal structure of K_2SiO_3 remains unavailable.

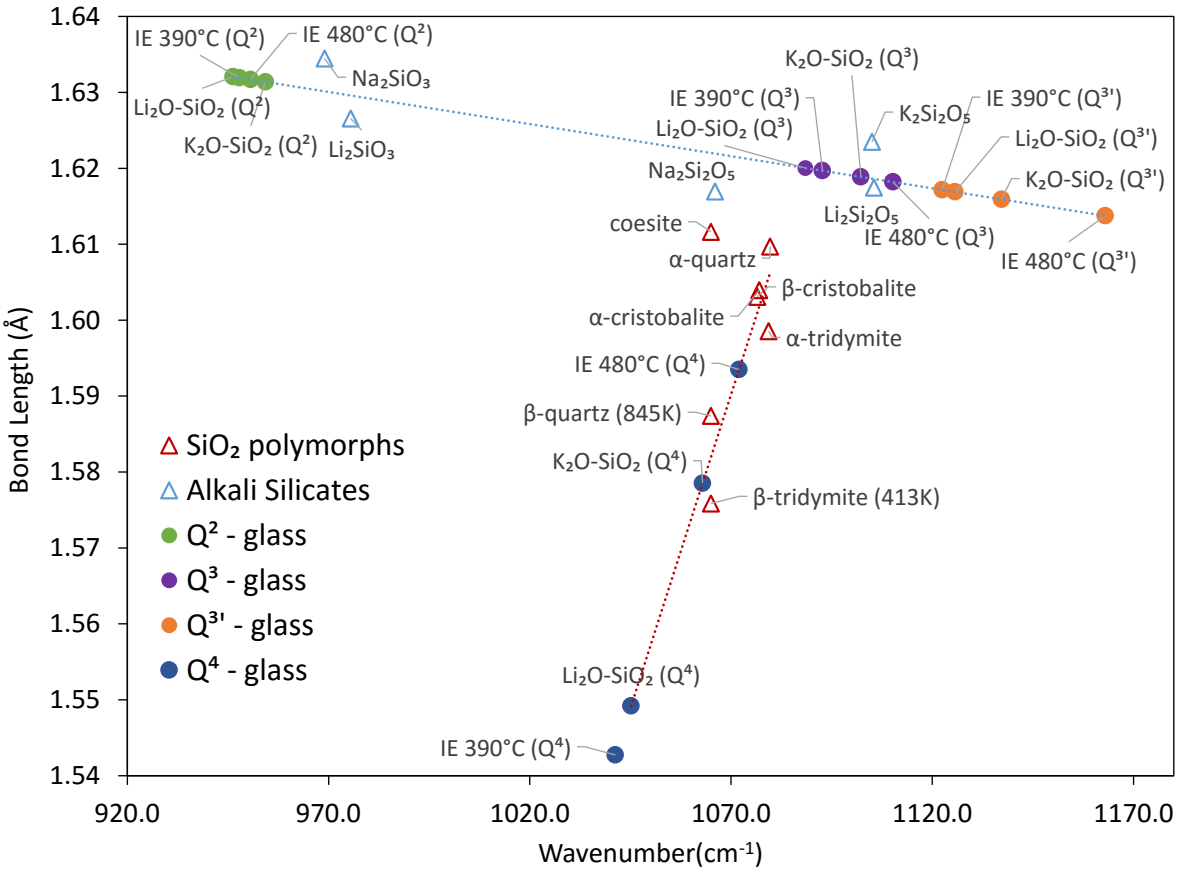

Figure 11: Calibration curve comparing average Si-O bond-length in crystal structures from literature to literature Raman data. Na_2SiO_3;[23,54–56] Li_2SiO_3;[23,56–60] $K_2Si_2O_5$;[23,61] $Na_2Si_2O_5$;[23,62,63] $Li_2Si_2O_5$;[23,60,61,64,65] coesite;[66–70,102] α-quartz;[69–86] α-cristobalite;[87–92] β-cristobalite;[89,91–94] α-tridymite;[95–97] β-quartz;[72,73,81,82,98–100] β-tridymite.[96,97,101] Literature values are available in the SI. SiO_2 polymorph crystals (△) line-of-best-fit, $R^2 = 0.83$, was used to calculate the corresponding Si-O bond-length for the Q^4-units(●) in the Li_2O-SiO_2, K_2O-SiO_2 and IE glasses from the measured Raman shift. High-pressure phases, coesite and stishovite, were excluded as they did not fit the trend. Alkali silicate crystals (△) line-of-best-fit, $R^2 = 0.63$, was used to calculate the corresponding Si-O bond-lengths for the Q^2(●), Q^3(●) and $Q^{3'}$-units(●) in the Li_2O-SiO_2, K_2O-SiO_2 and IE glasses from the measured Raman shift. Errors in $\langle d(\text{Si-O})\rangle$ determined from the fits are $\pm 5\times10^{-3}$ Å ($\pm 0.3\%$) for both Q^2 and Q^3-units, and $\pm 6\times10^{-3}$ Å ($\pm 0.4\%$) for Q^4-units. For the Raman and crystal data, at least two separate literature values were averaged; however, for α and β-tridymite has one experimental and one calculated value.[97] Additionally, the crystal data only contains one value for the structures of $K_2Si_2O_5$ and $Na_2Si_2O_5$. As of now, the crystal structure of K_2SiO_3 remains unavailable.

in SiO_2 polymorphs, where the bond-length is increasing with wavenumber is more difficult to explain. Using the trends in Fig. 11, $\Delta\nu$'s of the 480 °C sample (4, 22, 37 cm^{-1}) translate into a bond-length decrease of -5×10^{-4}Å (−0.2%), -2×10^{-3}Å (−0.1%) and -3×10^{-3} Å (−0.2%) for Q^2, Q^3 and $Q^{3'}$-units, respectively. Q^4-units, on the other hand, saw a large increase in Si-O bond-length of 4.43×10^{-1}Å (2.9%). A strain of 2.9% is larger than most in brittle ceramics, with the exception of structural phase transitions; otherwise, the material would fail much before those high of strains. Consequently, it seems like the structure of the IE-glass is changing as well as being strained, such as increasing the number of NBOs, in addition to a less electronegative K^+ replacing Li^+. In this case, temperature appears to have a linear effect on Si-O bond-length.

Relaxation Mechanisms

Plotting Si-O-Si bond-angle versus average Si-O bond-length of literature crystal data in Fig. 12, there appears to be a negative correlation for SiO_2 polymorphs and alkali silicates alike, such that as ∠SiOSi decreases, $\langle d(\text{Si-O})\rangle$ increases. Indeed, the IE glasses exhibit bond-angle reductions in Q^2 and Q^3-units concurrently with the lengthening of Q^4 d(Si-O). The Q^2 and Q^3-units neighbouring the ion-channels must accommodate the larger ion, both in space and coordination number, leading to reduction in network volume by collapsing the SiO_4 tetrahedra towards one another. IE likely causes the ion-channels within the glass to be more rigid than in the corresponding as-melted glass-structure, so it follows that the NBO or Si-O^- bond-lengths in Q^2 and Q^3-units are constrained and unable to dilate, while Q^4-units have more freedom. Consequently, the changes in ∠Si-O-Si in the Q^2 and Q^3-units necessitated by the larger invading ion are accommodated by dilation of the Q^4 network.

The IE-glass values determined from the Raman spectra in the previous section are included to demonstrate that they lie in the expected region of the graph compared to the crystal data. The Si-O-Si bond-angles of the Q^4-units are held constant since no correlation was found between Raman shift and ∠Si-O-Si; however, due to the relationship between ∠Si-

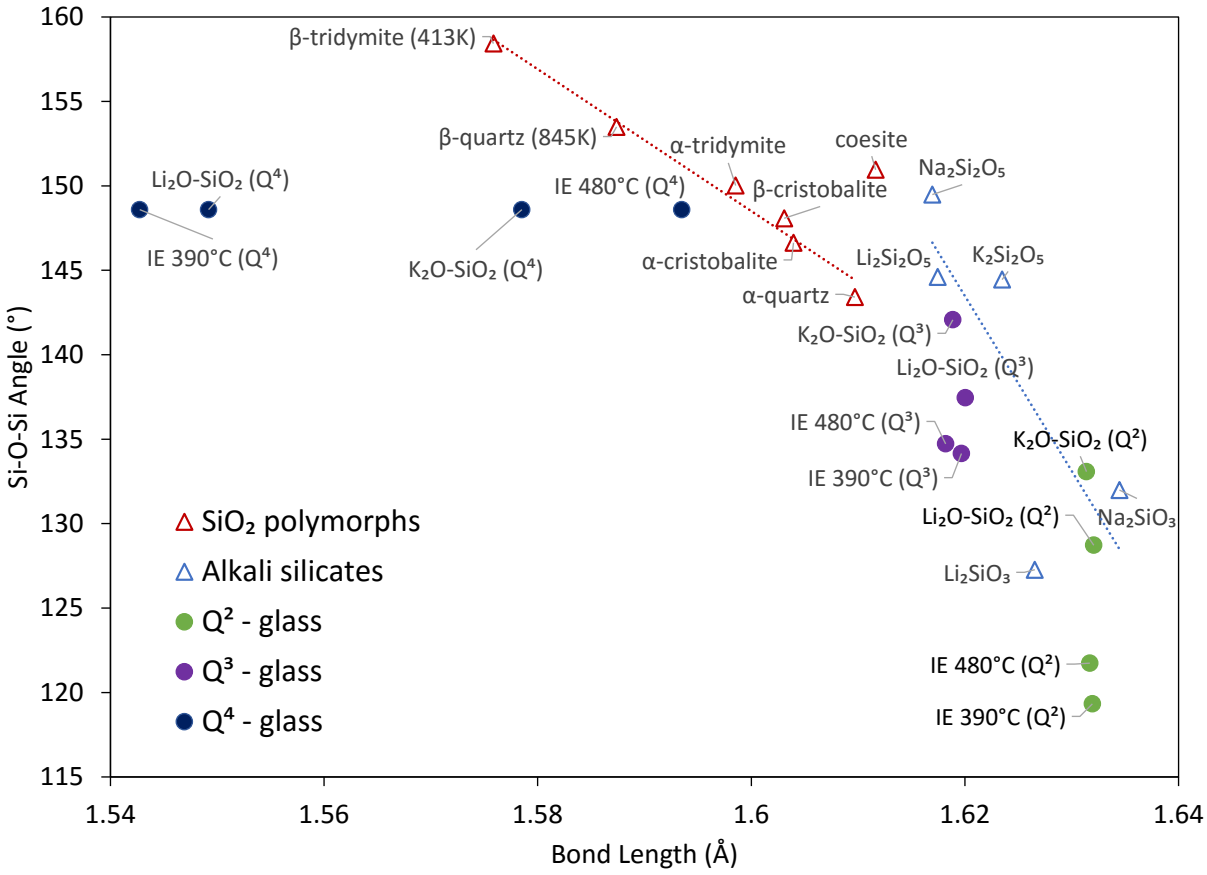

Figure 12: Relationship between average Si-O bond-length and Si-O-Si bond-angle in silicate crystal structures from literature. Na_2SiO_3;[54,55] Li_2SiO_3;[57–59] $K_2Si_2O_5$;[61] $Na_2Si_2O_5$;[62] $Li_2Si_2O_5$;[61,64,65] coesite;[66,67] α-quartz;[71–79] α-cristobalite;[87,88] β-cristobalite;[93,94] α-tridymite;[95–97,103] β-quartz;[72,73,98,99] β-tridymite.[96,101] At least two separate literature values were averaged for each crystal structure, wih the exception of $Na_2Si_2O_5$ and $K_2Si_2O_5$. The line-of-best-fit for SiO_2 polymorph crystals (△) has an $R^2 = 0.98$ (once the high-pressure phase coesite is removed), while the alkali silicate crystals' (△) trend has an $R^2 = 0.63$. This is simply to show a negative correlation between $\langle d(\text{Si-O})\rangle$ and ∠Si-O-Si, although there is a different relationship for Q^4-units(●) in comparison with Q^2(●) and Q^3-units(●). The $\langle d(\text{Si-O})\rangle$ and ∠Si-O-Si for Li_2O-SiO_2, K_2O-SiO_2 and the IE glasses are those calculated from the measured Raman shifts as shown in the previous section. As of now, the crystal structure of K_2SiO_3 remains unavailable.

O-Si and $\langle d(\text{Si-O})\rangle$, it may be fair to extend the negative correlation between ∠Si-O-Si and $\langle d(\text{Si-O})\rangle$ to Q^4-units as well. Nevertheless, all following calculations still hold the ∠Si-O-Si in Q^4-units to be constant.

Furthermore, calculations[49,104] have shown the ∠Si-O-Si to shift to smaller angles as R/r decreases, where R is the oxygen-second-nearest-neighbour-oxygen or O-Si-O separation and r is the Si-O bond-length, thus reinforcing the idea that ∠Si-O-Si and $\langle d(\text{Si-O})\rangle$ are negatively correlated. Hill and Gibbs similarly state that ∠Si-O-Si are determined by Si-O bond-lengths, d(Si-O), and Si-next-nearest-Si interactions, Si$\cdots$Si; larger Si$\cdots$Si-separations are correlated with longer d(Si-O) and larger ∠Si-O-Si, as fit in the following:[105]

$$\log d(\text{Si}\cdots\text{Si})/\text{Å} = \log 2\langle d(\text{Si}-\text{O})\rangle/\text{Å} + b\log\sin\left(\frac{1}{2}\angle\text{Si}-\text{O}-\text{Si}\right) \tag{4}$$

In fact, by assuming the variance in $d(\text{Si}-\text{O})$ is small and using the general relationship in Eq. 4, Hill and Gibbs found clear linear correlations for both crystalline SiO_2 polymorphs (N = 161, R^2 = 0.98) and alkali silicate crystals (N = 87, R^2 = 0.93) alike. Moreover, the authors found that the slope, b, differed very little for SiO_2 polymorphs and silicates, 0.808 in comparison to 0.809; hence, the relationship in Eq. 4 can be applied to all Q^n-species present in the IE glasses. As the d(Si-O) and ∠Si-O-Si have been determined from the Raman data using correlations in Figs. 10 and 11, it is now possible to calculate the changes in Si$\cdots$Si. To accomplish this, Eq. 4 must be modified using experimental Q^n-species fractions, x_{Q^n}, in addition to being summed over all possible Q^n-interactions, to obtain the average $\langle d(\text{Si}\cdots\text{Si})\rangle$ separation:

$$\log\langle d(\text{Si}\cdots\text{Si})\rangle = \sum_{o,p=2}^{4} x_{Q^o}x_{Q^p}\left[\log 2\langle d(\text{Si}-\text{O})_{Q^o}\rangle + 0.81\log\sin\left(\frac{1}{2}\angle\text{Si}-\text{O}-\text{Si}_{Q^p}\right)\right] \tag{5}$$

The $\langle d(\text{Si}\cdots\text{Si})\rangle$ separation was found by this approach to be 3.05 Å and 3.02 Å for untreated and 390 °C samples respectively; although 0.03 Å appears to be a small reduction in $\langle d(\text{Si}\cdots\text{Si})\rangle$, it results in an approximate 2% reduction in silica network volume, $\delta V_{\text{network}}$,

as determined by Eq.6.

$$\delta V/V^{\text{network}} = 3\frac{\langle d(\text{Si}\cdots\text{Si})\rangle - \langle d(\text{Si}\cdots\text{Si})\rangle_{\text{ref}}}{\langle d(\text{Si}\cdots\text{Si})\rangle_{\text{ref}}}, \tag{6}$$

where the reference state is the pristine middle section of each treated glass. The pristine middle sections of the high temperature IE treatments, 450 and 480 ° were found to change structurally, compared to the untreated 30% Li_2O glass. The $\delta V/V^{\text{network}}$ results for all IE samples, untreated and 360–490 °C are shown in Fig. 13. The network is seen to densify at low IE temperatures, 390–420 °C, and then at IE temperatures $\geq T_g$, relaxation and expansion occur due to larger K^+-ions entering. In fact, IE temperatures near or above T_g, 450 and 480 °C, show a large increase in network volume near the edge, indicating large structural rearrangement.

It is difficult to estimate the stress present in IE-glass without measuring it directly, however, to a first approximation, the reduction in $\text{Si}\cdots\text{Si}$ separation can be thought as the result of an uniformly applied stress. Since the surface is free to move, the stress is anisotropic, however, we are only able to measure the volume change and must treat the stress as hydrostatic. In this case we can estimate the stress σ as $\delta P/3$, where δP is the effective hydrostatic pressure due to the IE process, and use the bulk modulus $\kappa = -\delta P/(\delta V/V)$ together with Eq. 6 to estimate stress. For the value of the bulk modulus we use the value of the 20% Li_2O- 10% K_2O bulk glass as representative. It is then possible to compare the results determined here to stresses reported in literature.[1,6] In this case, we are assuming the ion volumes stay constant and do not participate in the stress. Fig. 14 shows the calculated axial stress for all IE-samples. First of all, these values are in good agreement with literature, which reports compressive stresses of approximately 350–970 MPa.[1,5,6,17] Our data agrees with literature expectations,[5] where the maximum compressive stress was found in the lowest temperature sample in which significant concentration of K^+ entered, in this case, 390 °C. Since the current IE procedure was done at higher temperatures relative

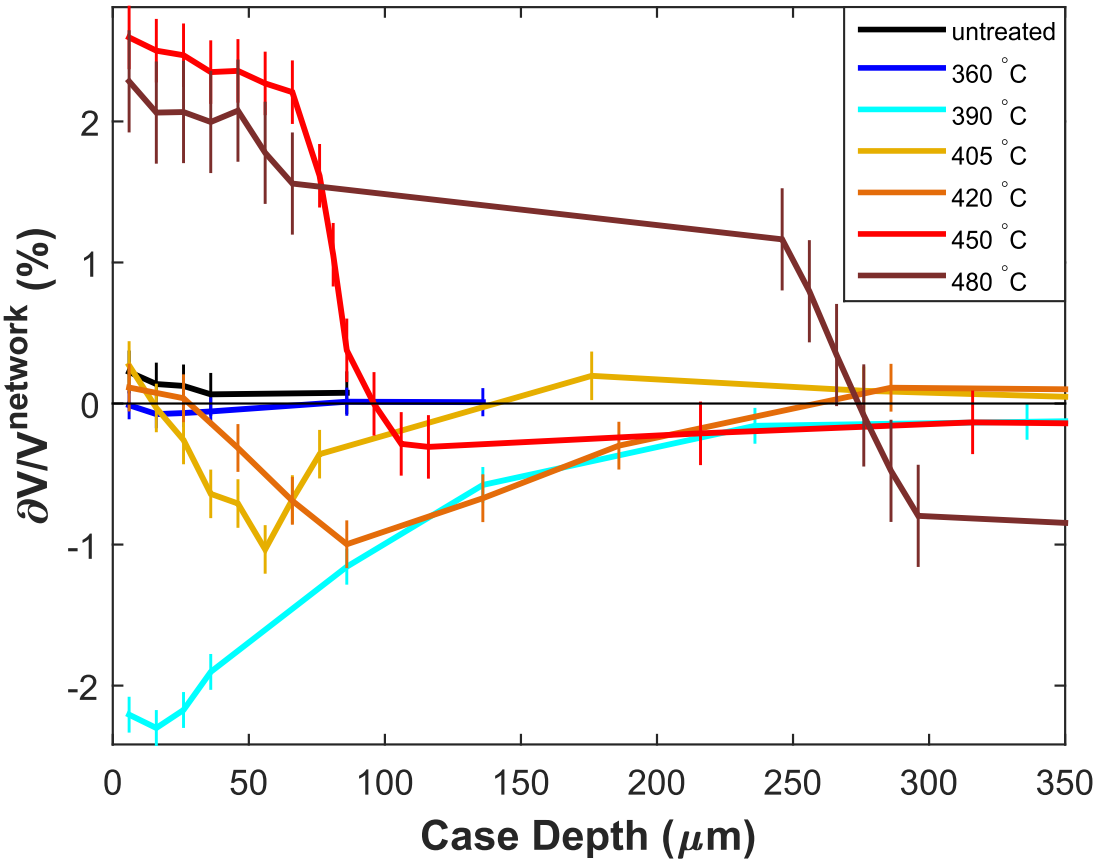

Figure 13: Relative densification or reduction in molar volume of the silica network, $\delta V/V^{\text{network}}$, determined from Eq. 6 as a function of distance from the IE-edge and IE-temperatures, untreated (black) and 360–480 °C (purple–red).

to T_g than in commercially available IE glasses, it is not surprising that the highest stress determined solely from the Raman spectra, $\approx$ 300 MPa, is at the lower end of literature values.

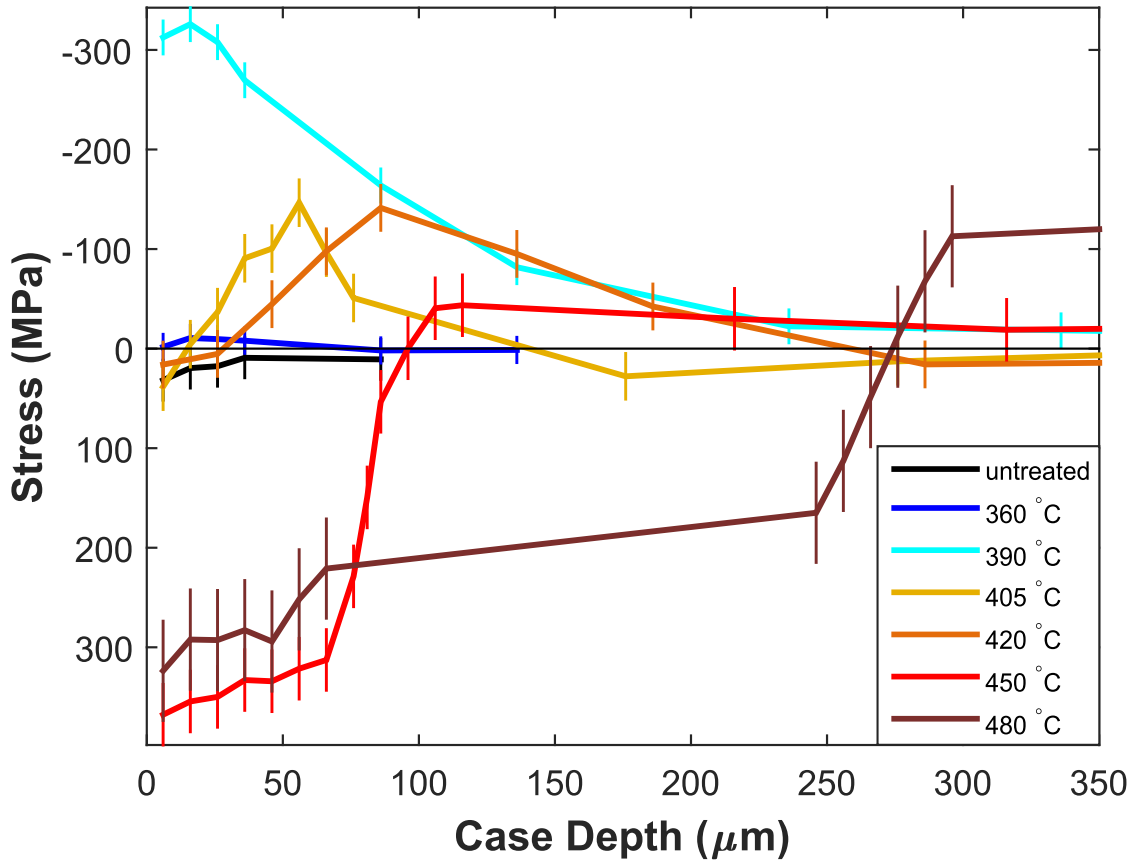

Figure 14: Axial stress along one dimension, σ_{ii}, determined from Eq. 2 as a function of distance from the IE-edge and IE-temperatures, untreated (black) and 360–480 °C (purple–red).

Secondly, Figs. 13 and 14 reveal a more complete understanding of the structural mechanisms than the shifted Raman shift, $\Delta\nu_c$, plots alone, Figs. 8 and 9. In general, the ν_c's linked to d(Si-O) increase dramatically with higher temperatures, while ν_c's linked to $\angle$SiOSi stay relatively constant as a function of temperature. The reduction in $\angle$SiOSi occurs as soon as any invading ion is present, even at lower temperatures, while the lengthening of d(Si-O) is a relaxation mechanism that can only occur when enough energy is present in the network. Furthermore, the effects of temperature and relaxation can be seen in Figs. 13

and 14, where the most densification or maximum compressive stress is seen to be lower and progressively further from the IE surface with increasing temperature. Although the ∠SiOSi for Q^4-units is not known and held constant, it is likely that an increase in average d(Si-O) would facilitate a decrease in ∠SiOSi as indicated by the trend in Fig. 12; this makes the estimate of the reduction in network volume conservative as it does not include reduction of the Q^4 ∠SiOSi. Since Fig. 13 shows there to be an expansion of the network at high IE temperatures, Fig. 14 shows a large tensile stress as a result, which may be overestimated since the structure was seen to clearly change at IE temperatures $\geq$ 450 °C. On the hand, the 480 °C sample was observed to have cracking after the IE process, so perhaps this is indicative of the large tensile stresses formed at the edge. It could also be mismatch between thermal expansion coefficients of Li- and K-containing regions,[106,107] although we expect the effect to be small in comparison to the compressive stress from the compositional effects. We are currently analyzing ellipsometry data to see if these calculated stresses in Fig. 14 match what is seen experimentally, nonetheless, the reduction and migration of maximum stress from the edge has been well-documented.[2,5,15]

This compaction followed by dilation of the silica network may indeed be the two-step relaxation process discussed earlier:[16,20] a fast local rearrangement followed by a slow relaxation towards the structure of the as-melted potassium end-member. However, the data presented here indicate the reverse order of rearrangements; rather than an expansion followed by an irrecoverable densification, an elastic compaction, i.e., Si-O-Si bond-angle reduction, followed by a plastic dilation, i.e., Si-O bond-lengthening at higher temperatures, is observed. This disagreement may be explained simply by noting re-orientation of SiO_4 tetrahedra requires less energy than bond-length changes. The first step likely involves non-linear elasticity, where the deformation would recover entirely on laboratory-length time scales if the load is removed.[16] This is solely based on the fact that there appears to be a preferred relationship between ∠SiOSi to d(Si-O) as shown in Fig. 12, which leads to the conclusion that the compressive stress manifested as reduction in ∠SiOSi may be relieved in one of two ways: either

the load can be removed and the ∠SiOSi returned to the "rest" position, or the d(Si-O) can increase. Finally, this relaxation mechanism may, in conjunction with viscous flow at the IE temperature, be an explanation for the lower-than-expected stress commonly seen in IE glasses, where the practically achievable compressive stress is significantly lower than that predicted from the as-melted composition.[16] There may exist a temperature-dependent stress threshold, where when breached, the structure yields and lengthens the d(Si-O) in response.

Linear Network Dilation Coefficient

Although $\delta V/V^{\text{network}}$ determined from the reduction in average $d(\text{Si}\cdots\text{Si})$ separation is a reasonable measurement of changes in the silica network, it does not describe the change in molar volume due to the volumes of the ions. The *total* molar volume, V_M^{total}, is a combination of the densification of the network as well as the volume increase expected from $\text{Li}^+ \leftrightarrow \text{K}^+$ substitution. We estimate the relative change in total molar volume, $\Delta V_M/V_M$, by summing the weighted relative changes in partial molar volumes V_M^i between the IE and bulk of each glass component, SiO_2, Li_2O and K_2O. For the silica contribution we use $\delta V/V^{\text{network}}$ from Eq. 6. We assume the lithium oxide contribution, $\Delta V_M^{\text{Li}_2\text{O}}$ between IE and bulk environments, to be negligible because the environments of lithium in the IE layer and lithium in the bulk glass should be quite similar. For potassium we estimate the change in partial molar volume, as potassium substitutes for lithium, as approximately $V_M^{\text{K}_2\text{O}} - V_M^{\text{Li}_2\text{O}}$. The result is

$$\frac{\Delta V_M}{V_M} \approx x_{\text{SiO}_2}\delta V/V^{\text{network}} + x_{\text{K}_2\text{O}}\frac{V_M^{\text{K}_2\text{O}}(\text{bulk}) - V_M^{\text{Li}_2\text{O}}(\text{bulk})}{V_M}. \tag{7}$$

Now it is possible to determine the LNDC (B) in Eq. 1 by plotting $\frac{1}{3}\Delta V_M^{\text{total}}$ versus mol-fraction of K_2O ($x_{\text{K}_2\text{O}}$ or $C_{\text{K}^+}(z)$); Fig. 15 compares the LNDC for the as-melted mixed-alkali series with increasingly higher-temperature IE glasses. It is clear that the IE-samples have a much shallower slope than the corresponding as-melted series because of the limited

relaxation of the network during IE. The final B values and R^2 values are tabulated in Table 4, which shows B to be quite close to what is expected from the literature,[2,16,17] roughly 2–4 times smaller compared with the as-melted mixed-alkali series.

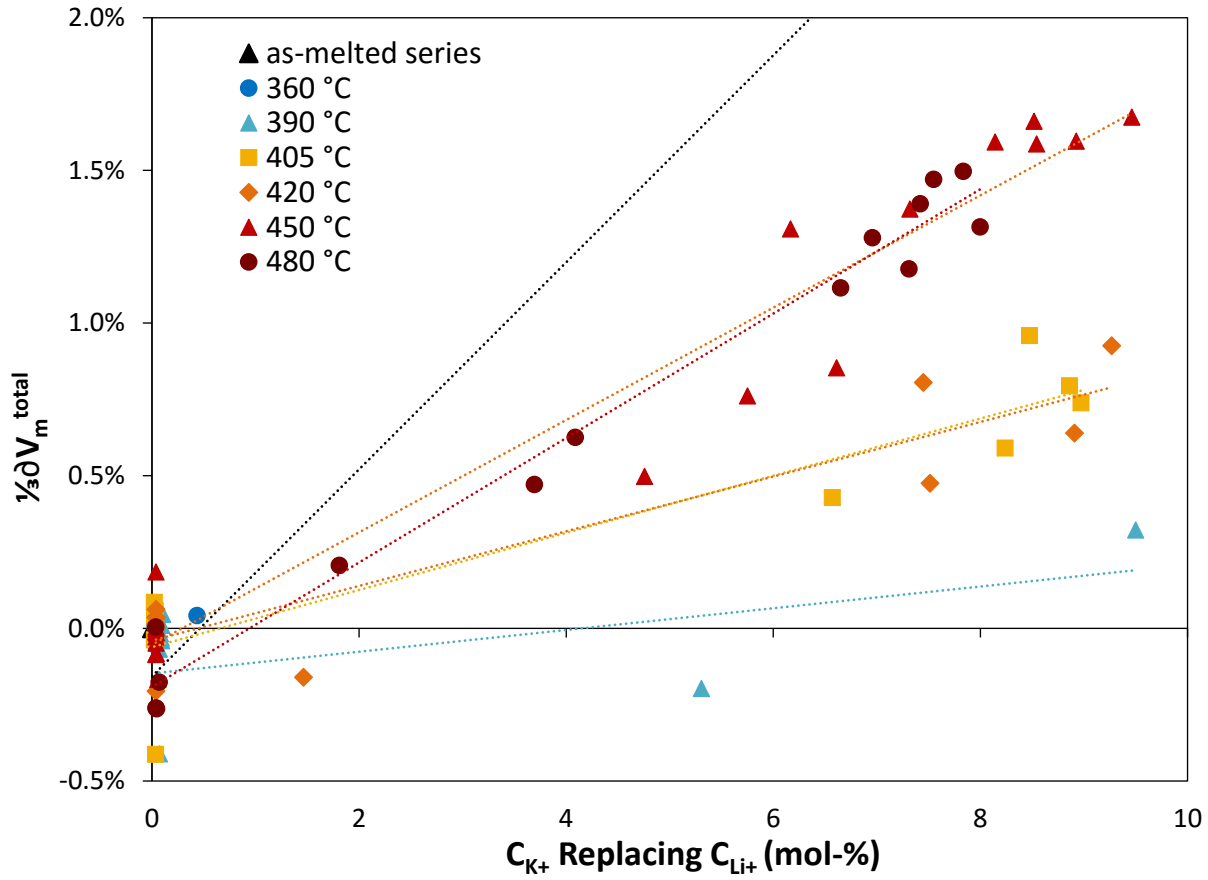

Figure 15: Determination of LNDC using Eq. 7 for all IE-temperatures, untreated (black) and 360–480 °C (purple–red).

The LNDC appears to depend positively on IE-temperature, indicating $\Delta V_M^{\text{total}}$ is more sensitive to K_2O content at higher temperatures. For example at equal concentrations of the substituting K^+-ions, $C_{K^+} \approx 10$, the $\Delta V_M^{\text{total}}$ is larger at 480 °C in comparison to the 405 °C sample. This result is consistent with the proposed mechanism for stress manifestation during $Li^+ \leftrightarrow K^+$ exchange: an initial reduction in Si$\cdots$Si separation caused by reduction in ∠SiOSi followed by an increase in Si$\cdots$Si separation due to lengthening of d(Si-O). The LT samples (390–425 °C) show only a small increase in $\Delta V_M^{\text{total}}$ with increasing K^+ concentration, indicating that the network densifies (by decrease of ∠SiOSi) to accommodate the increased

Table 4: LNDC or B,[2,19] error (ΔB) and correlation-coefficient (R^2) calculated using bulk Li_2O as the reference (Eq. 7 and Fig. 15) for as-melted series in comparison with IE glasses at increasing temperatures

Sample	B (mol-% K_2O)$^{-1}$	ΔB (mol-% K_2O)$^{-1}$	R^2
xLi_2O-(30−x)K_2O-70SiO_2	3.4×10^{-3}	2×10^{-4}	0.994
390 °C	6×10^{-4}	2×10^{-4}	0.65
405 °C	9×10^{-4}	1×10^{-4}	0.85
420 °C	1.0×10^{-3}	2×10^{-4}	0.85
450 °C	2.0×10^{-3}	1×10^{-4}	0.95
480 °C	2.04×10^{-3}	6×10^{-5}	0.98

volume of the invading ion and that little structural relaxation (i.e., increase in $\langle d(\text{Si-O})\rangle$) occurs. Additionally, the lower correlation coefficient for these LT samples can be explained by the antagonistic two-step process. The increase in structural relaxation with temperature can explain the temperature-sensitivity of the LNDC in Fig. 15 and Table 4.

Another consequence of the LNDC anomaly is manifested when compressive stress is calculated using B in Eq. 2: if the LNDC for the as-melted mixed-alkali series is used, the compressive stresses obtained are also 2–4 times higher than the stresses measured photoelastically in IE glasses.[2,16–18] To illustrate this point further, Fig. 16 shows the stress, $\sigma(z)$, calculated using Eq. 2, with B determined from $\Delta V_M^{\text{total}}$ in Eq. 7 and the mol-fraction of K^+, $C_{K^+}(z)$), from WDS . Studies of IE glasses have shown tension of < 100 MPa past the case depth,[2] therefore, the average mol-fraction of K^+, C_{avg}, was artificially set to generate tension between 10–50 MPa. This is simply extending the sampling range beyond what was measured using WDS, for example, a longer distance would result in a lower average mol-fraction of K^+, C_{avg}.

Fig. 16, by comparison to Fig. 14 shows how Eq. 7 overestimates the stress at the IE surface, since it equates a positive $\partial V_M^{\text{total}}$ to compressive stress, but if lengthening Si-O bonds are indeed a relaxation mechanism, that is not always the case. Overall, the molar volume will always increase compared to the untreated lithium silicate due to larger ions filling smaller interstices, as shown by finite element modelling,[2] but a larger $\Delta V_M^{\text{total}}/\Delta C_{K^+}(z)$ means more relaxation has occurred and less compressive stress is present. This can be seen clearly in

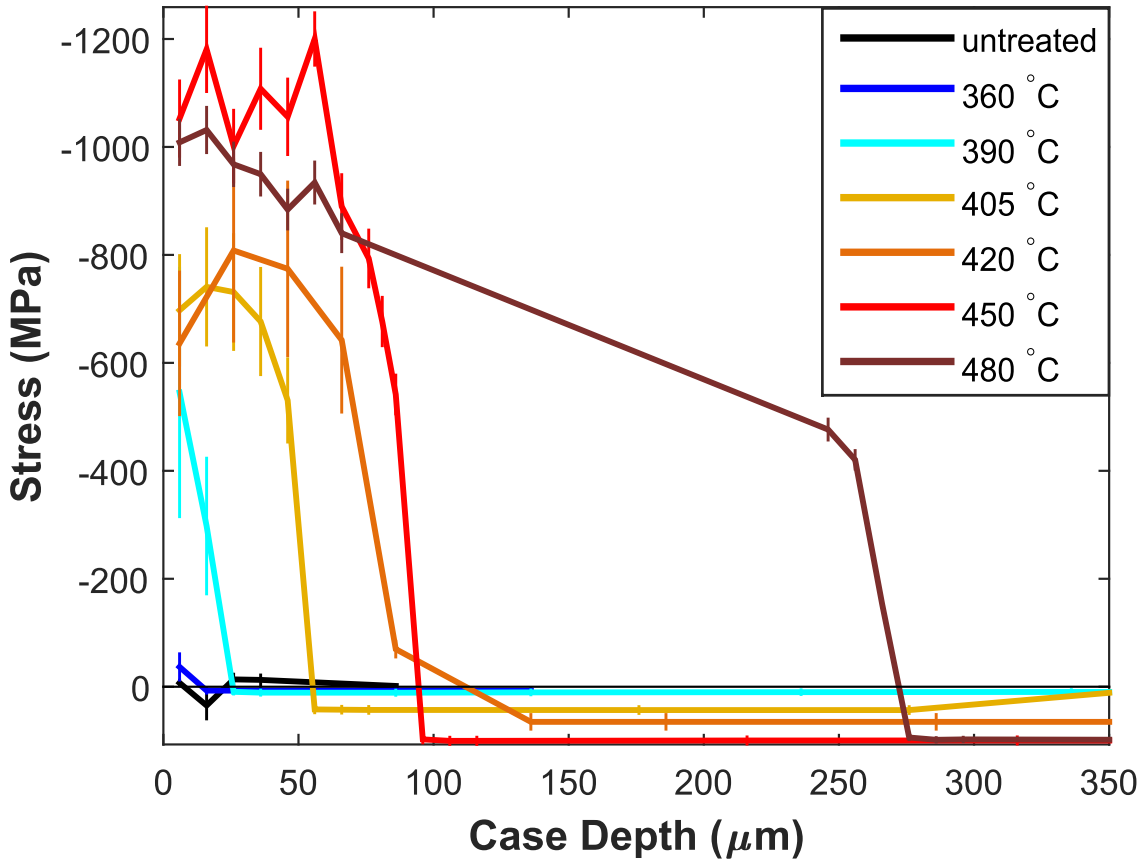

Figure 16: Stress determined from Eq. 2 and B when bulk Li_2O is the reference state (from Eq. 7 and Fig. 15), as a function of case depth for all IE-temperatures, 360–480 °C (purple–red).

Fig. 15, where the highest temperature IE sample with the largest thermal relaxation also has the largest value of $\Delta V_M^{\text{total}}/\Delta C_{\text{K}^+}(z)$. Additionally, Eq. 2 likely underestimates the stress at low temperatures, since the total molar volume, $\Delta V_M^{\text{total}}$, is similar to the initial untreated molar volume resulting in a small B, yet the Raman data shows the silica network to be stressed and densified due to dilation of the ion channels.

The method of estimating stress from the change in molar volume per change in alkali ion from a bulk lithium-modified glass does not account for the reduction in network molar volume that occurs from compressive stress. The IE glass with the highest maximum compressive stress is one where there is no change in molar volume compared to the untreated sample, indicating the silica network has densified without being able to relax (that is, a decrease in ∠SiOSi with no relaxation in Si-O bond lengths). For the IE structure to have the most stress, it should be furthest from its equilibrium state, i.e., the as-melted mixed-alkali composition corresponding to the final IE composition, not the initial untreated structure. In such a state the partial molar volume of K_2O would be quite similar to what it is in a pure potassium silicate glass. It is therefore interesting to consider an alternative method of determining B, using $V_M^{\text{K}_2\text{O}}$(bulk) as the reference state:

$$\frac{\Delta V_M}{V_M} \approx x_{\text{SiO}_2}\delta V/V^{\text{network}} + x_{\text{K}_2\text{O}}\Delta_K. \tag{8}$$

Here ΔK is the reduction in molar volume for K^+ in the IE layer compared to in a relaxed K^+ site. The similar factor in Eq. 7 was the difference between a relaxed K^+ site and a Li^+ site, which is clearly large and positive.

The closer the IE structure is to the as-melted mixed-alkali structure, the less stress is present in the glass. If we calculate B using $\frac{1}{3}\Delta V_M^{\text{total}}$ determined from Eq. 8 and an estimate of $\Delta_K \approx -0.1$, we obtain an LNDC that changes from negative to positive with increasing temperature, shown in Fig. 17. The exact B values when the K_2O reference is used are tabulated in Table 5. When the glass is stressed the first and second terms are negative,

however, at higher temperatures, the network is no longer densifying, in fact, $\Delta V_M^{\text{total}}$ is positive, thus, there is a sign change despite the second term remaining negative. Although counter-intuitive, the LNDC is negative at low IE temperatures because the reference state is bulk K_2O; it is a direct result of the network densifying and $V_M^{K_2O}(\text{IE}) \leq V_M^{K_2O}(\text{IE})$. Furthermore, $\frac{1}{3}\Delta V_M^{\text{total}}$ always remains below zero; in fact, high IE temperatures 450 and 480 °C are seen to approach zero or equilibrium V_M of the as-melted $20Li_2O$-$10K_2O$-$70SiO_2$ composition. Additionally, the IE glass always has a larger V_M^{total} than that of the untreated 30% Li_2O glass, which has a $\frac{1}{3}\Delta V_M^{\text{total}}$ of -3.0% relative to the as-melted $20Li_2O$-$10K_2O$-$70SiO_2$ composition. The high temperature IE treatments show the structure to densify, *i.e.*, have larger $\frac{1}{3}\Delta V_M^{\text{total}}$, significantly. Overall, in either reference state, bulk Li_2O (*see Eq. 7*) or K_2O (*see Eq. 8*), *lower* values of the LNDC should be equated with more compressive stress, rather than higher values per Eqs. 1 and 2.

The stress determined from Eq. 2 using the alternative B with bulk K_2O as the reference is shown in Fig. 18. In this alternative formulation, Eq. 2 does not include the negative sign in the front, to account for the change in perspective from K^+ addition to K^+ deletion. The change in reference state gives a stress profile which matches quite well with the experimental profile measured from the Raman data (Fig. 14) as well as what is expected from literature: the stress maximum decreases and migrates inwards with increasing IE temperature. The change in sign for B allows for the complex behaviour expected in the stress profile. This reformulation ensures that a compressive stress or decrease in ${\Delta V_M}^{\text{total}}$ always exists for the ion interstice (although that may not be true at high IE temperatures like 450 and 480 °C) and most importantly allows the direction of the $\Delta V_M^{\text{network}}$ to be significant, rather than overwhelmed by the increase in ion volume when bulk Li_2O is used as the reference state.

As mentioned before the maximum achievable stress occurs when the most ion-exchange has occurred without expansion, thus, an IE glass with a similar molar volume to the starting material should have the most enhanced mechanical properties. This condition puts a lower bound on possible molar volume, since the IE volume cannot be smaller than the starting

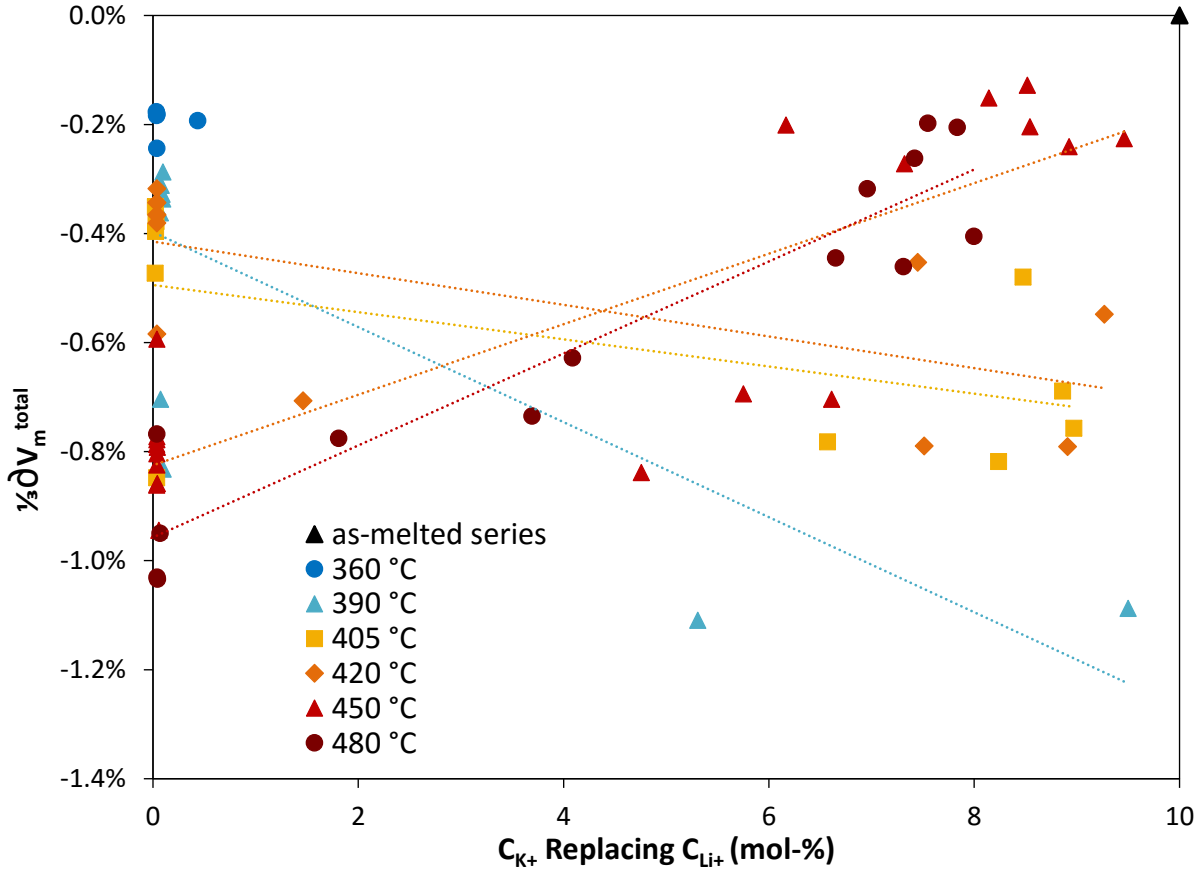

Figure 17: Determination of LNDC, B, using Eq. 8 and mol-% of substituting ion, K^+, (from WDS) for all IE temperatures, untreated (black) and 360–480 °C (purple–red).

Table 5: LNDC or B,[2,19] error (ΔB) and correlation-coefficient (R^2) calculated using bulk K_2O as the reference (Eq. 8 and Fig. 17) for as-melted series in comparison with IE glasses at increasing temperatures

Sample	B (mol-% K_2O)$^{-1}$	ΔB (mol-% K_2O)$^{-1}$	R^2
xLi_2O-$(30-x)K_2O$-$70SiO_2$	3.4×10^{-3}	2×10^{-4}	0.994
390 °C	-6×10^{-4}	3×10^{-4}	0.64
405 °C	-2×10^{-4}	1×10^{-4}	0.36
420 °C	-2×10^{-4}	2×10^{-4}	0.21
450 °C	7.7×10^{-4}	1×10^{-4}	0.75
480 °C	8.5×10^{-4}	8×10^{-5}	0.90

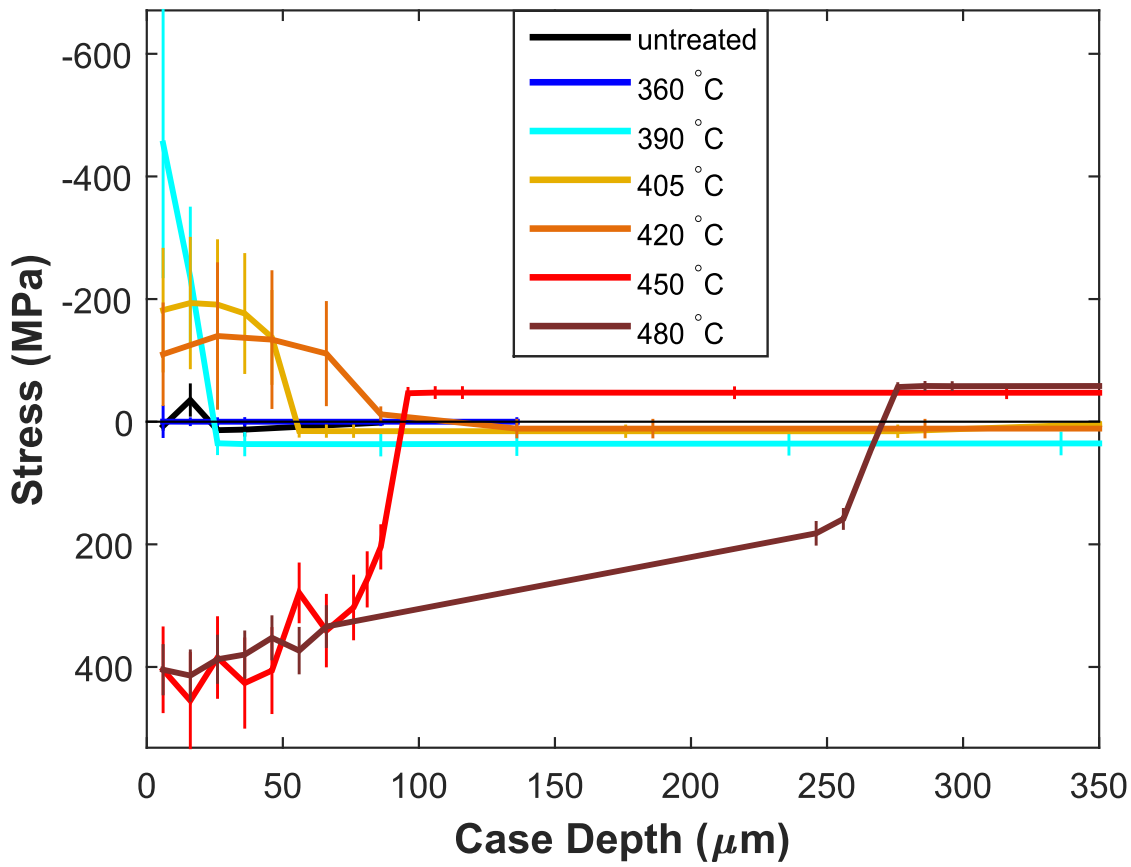

Figure 18: Stress determined from Eq. 2 and B when bulk K_2O is the reference state as a function of case depth for all IE-temperatures, 360–480 °C (purple–red).

volume as well as a corresponding higher bound on *possible* compressive stress. As a result, using a *bulk* as-melted glass system with a higher LNDC may appear beneficial to achieving more stress, since there would be a larger difference in molar volume between the starting and equilibrium structure. However, that difference is only the *possible* compressive stress, not necessarily what is achievable through IE. For example, let us consider two different glass systems, alkali aluminosilicate versus alkali silicate, where the LNDC of the *bulk* as-melted mixed-alkali aluminosilicate series in lower than the corresponding silicate series, yet the aluminosilicate series has higher, almost double, compressive stress.[18] It is possible to have a system where upon the addition of the larger ion, the molar volume of the IE glass is increasing at a slower rate compared to its as-melted equilibrium structure, only the *difference* between the two structures matters, so a system can still have a lower as-melted LNDC and higher compressive stress. Additionally, aluminosilicate crystals and glasses are known to be stiffer than corresponding silicate crystals[108] and glasses.[109,110] In fact, the higher stiffness of the aluminosilicate network may be responsible for its lower LNDC; a more rigid network may result in a smaller molar volume change as a function of mixed composition. Since stiffness converts strain to stress, it is important to consider the strain, i.e., the reduction in molar volume compared to the equilibrium structure, as well as the stiffness when determining the compressive stress. Thus, the structure with the most achievable stress must have the largest difference in V_M between the IE and equilibrium structure as well as the highest stiffness.

The difficulty with comparing these results with literature stems from the fact that experimental studies are limited to calculating B from the measured stress using Eq. 1, so they obtain a higher B for a higher measured stress.[2,18] On the other hand, computational studies obtain B from the molar volume change in Eq. 1, however, these studies have great trouble calculating reasonable stresses, since IE glasses are "forbidden glasses" where the structure is not achievable through thermal routes alone.[16,17,22,111] The current study uniquely provides a method to experimentally determine the changes in molar volume of the silica network during the IE process which can be spatially compared to the expected compressive stress

profile.

Nonetheless, proof of a lower LNDC for the IE glass in comparison to the as-melted value indicating higher compressive stress may be found in how the LNDC depends logarithmically on the amount of ion-exchange which has occurred. Many studies have considered the dependence of the LNDC on the starting fraction of K_2O in the untreated glass (larger starting K_2O-fraction means less IE can occur); the LNDC has been shown computationally[16,20,22] and experimentally[18] to vary more when only small amounts of alkali have been exchanged, while at high amounts of exchange, B is fairly constant. All other things being equal, time and temperature for each starting composition, we would expect the greatest compressive stress to be found at the largest amount of ion-exchange; this is also where B is not changing greatly with amount of IE. A structure with the most stress and an invariant B while exchange occurs would indicate a structure whose molar volume is unchanging despite larger ions being present. One computational study[22] found Young's modulus to depend positively on the amount of exchange, i.e., concentration of K^+, despite B remaining constant at high amounts of exchange, proving further the most enhanced mechanical properties occur where the most ion-exchange has occurred *without* an increase in expansion. The explanation as to why B varies so much at small amounts of ion-exchange may simply be that there is some ability for the network to expand elastically and accommodate the larger invading ions, as is proposed by many authors,[16,31,31] however, very quickly the critical volume is reached and the network must densify to accommodate the larger ions.

Conclusion

The structure of an ion-exchanged glass was probed using micro-Raman spectroscopy and compared to the compositionally-equivalent as-melted mixed-alkali series, xLi_2O-$(30-x)K_2O$-$70SiO_2$. The Q^ndistribution in the IE glasses exhibited conversion of Q^2-units and Q^4-units to Q^3 as IE progressed, additionally, a net conversion of BOs to NBOs was observed at tem-

peratures near or above T_g . The identified Raman peaks were shown to shift the most for high-temperature samples, indicating a positive correlation between temperature and structural modifications. Additionally, the low-frequency region Raman peaks known to correlate with external Si-O-Si bond angle showed a decrease in bond angle for Q^2 and Q^3-units as a function of K^+ concentration or exchange depth, a maximum of $-9.4°$ (-7.3%) and $-3.3°$, (-2.4%), respectively for the lowest IE-temperature where exchange occurred, 390 °C. On the other hand, the peaks corresponding to Q^4 $\angle$SiOSi did not change significantly following ion-exchange. The high-frequency region peaks showed an increase in wavenumber, indicating a slight shortening of average Si-O bond-length for Q^2 (-0.02%) and Q^3-units (-0.1%) and substantial lengthening in Q^4-units ($+2.9\%$) at high temperatures, while low-temperatures and far enough from the IE surface in high-temperatures displayed much less significant modification of the $\langle d(\text{Si-O})\rangle$.

The calculated $\angle$SiOSi and $\langle d(\text{Si-O})\rangle$ were used to calculate the Si$\cdots$Si separation, which was treated as being equivalent to network molar volume. By comparing the IE samples with the untreated material, $30Li_2O$-$70SiO_2$, the reduction in network molar volume was used along with the bulk modulus to determine the compressive axial stress, which exhibited trends similar to experimental stress profiles. The subsurface maximum stress both decreased and migrated inward as temperature increased. Additionally, the calculated maximum stress was similar to reported values and was found at the lowest temperature where significant IE occurred. A two-step structural modification process is proposed, where at low-energy conditions, i.e., well below T_g or at low concentrations of substituting ion, the network tetrahedra collapse towards each other, leading to reduction in Si$\cdots$Si separation or silica network volume; however, above the energy-threshold, the Si-O bonds lengthen in order to relax some of the compressive stress which leads to a much less-reduced network molar volume. This analysis has demonstrated that micro-Raman spectroscopy could be used as a rapid in-situ measurement tool for the determination of stress in IE glass.

When the increase in cation interstice size was included in the molar volume calculation,

LNDCs for the IE glasses were determined and found to match those reported in literature. Additionally, a second stress profile was determined using the LNDCs, showing more clearly that the LNDC model overestimates stress at temperatures near or above T_g and underestimates it when well below T_g. Since the LNDC depends directly on molar volume, it does not account for the first-step in the structural rearrangement process, i.e., the reduction of the network molar volume due to compressive stress. The current LNDC model uses the bulk lithium silicate structure as the reference equilibrium state, however, when bulk potassium silicate was used instead, a more realistic stress profile was obtained. This change of reference state demonstrates how an IE glass with a *higher* LNDC has relaxed towards to the equilibrium state and will have *less* compressive stress, rather than more σ as is currently predicted. The maximum *possible* stress exists when the most ion-exchange has occurred without expansion, however, the *actual* compressive stress is a function of the *difference* between the molar volume of the IE and equilibrium structure as well as the stiffness of the network. The underestimation of stress in IE glass by the LNDC model could have important implications for the prediction of stress in commercial IE glass.

Overall, the Raman data show evidence for two different structural-alteration regimes for a lattice under compression: decreased external Si-O-Si bond-angles followed by increase in Si-O bond-length. This may indicate a limit of the maximum stress achievable through ion-exchange; it appears that once the strain limit is reached, the material relaxes and reduces the compressive stress accordingly. Moreover, the higher temperatures required to exchange the ions deeper into the material could aid structural relaxation. Nonetheless, this phenomenon may be unique to silicate structures and other glass network-formers, such as aluminosilicates which show twice the compressive stress, should be examined for similar trends.

Associated Content

Supporting Information

This material is available free of charge at http://pubs.acs.org/. Raman spectra at treated edge in comparison with bulk glass, for high and low temperture exchange treatments; wavenumber shifts of major Raman features; detailed fits showing deconvolutions; detailed comparison of spectral features in treated versus untreated samples; silica site fractions as a function of case depth; atomic composition as measured by WDS as a function of case depth; shifts in bond lengths and angles as extracted from the Raman data as a function of process temperature; tables of Raman shifts from glass samples and tables of literature Raman data in silicates used for comparison and extraction of bond length and angle shifts.

Acknowledgement

Financial support from the Natural Sciences and Engineering Research Council of Canada (Canada Grant Number RGPIN 261987) is gratefully acknowledged. We appreciate the assistance of Dan MacDonald for his work on the WDS elemental analysis, and Carl Romao for many helpful discussions and criticisms.

References

(1) Gy, R. Ion Exchange for Glass Strengthening. *Mater. Sci. Eng. B* **2008**, *149*, 159–165.

(2) Varshneya, A. K. Chemical Strengthening of Glass: Lessons Learned and Yet To Be Learned. *Int. J. Appl. Glass Sci.* **2010**, *1*, 131–142.

(3) Rogoziński, R. In *Ion Exchange Technologies*; Kilislioğlu, A., Ed.; Intech, 2012; pp 154–190.

(4) Stavrou, E.; Palles, D.; Kamitsos, E. I.; Lipovskii, A.; Tagantsev, D.; Svirko, Y.;

Honkanen, S. Vibrational Study of Thermally Ion-exchanged Sodium Aluminoborosilicate Glasses. *J. Non-Cryst. Solids* **2014**, *401*, 232–236.

(5) Sane, A.; Cooper, A. Stress Buildup and Relaxation during Ion Exchange Strengthening of Glass. *J. Am. Ceram. Soc.* **1987**, *70*, 86–89.

(6) Varshneya, A. K. Method for Making Strengthened Glass. US Patent 8959953, 2015.

(7) Huang, M. Stress Effects on the Performance of Optical Waveguides. *Int. J. Solids Struct.* **2003**, *40*, 1615–1632.

(8) Saitoh, K.; Koshiba, M.; Tsuji, Y. Stress-Analysis Method for Optical Waveguides Composed of Elastically Anisotropic Materials and Its Application to Strain-induced Optical Waveguides. *Electron. Comm. Jpn. 2* **1998**, *81*, 16–23.

(9) Kurkjian, C. R.; Kammlott, G. W.; Chaudhri, M. M. Indentation Behavior of Soda-Lime Silica Glass, Fused Silica, and Single-Crystal Quartz at Liquid Nitrogen Temperature. *J. Amer. Ceram. Soc.* **1995**, *78*, 737–744.

(10) Gonella, F.; Quaranta, A. On the Recovery of Refractive-index Profiles of Ion-exchanged Glass Waveguides. *Pure Appl. Opt.* **1993**, *2*, 405–409.

(11) Gonella, F.; Caccavale, F.; Quaranta, A.; Sambo, J. Copper-doped Ion-exchanged Waveguide Characterization. *J. Mod. Opt.* **1998**, *45*, 837–845.

(12) Lee, J. C. Effects of Exchange Temperature on Properties in Field-assisted Ion-exchanged Glass. Ph.D. thesis, Iowa State University, Ames, Iowa, 1986.

(13) Varner, J.; Lang-Egelkraut, R. Influences of Ion-Exchange Temperature and Time on Stress Profiles and Strengths of Chemically Strengthened Glass. Proc. Fourth Intl. Conf. on the Physics of Non-Crystalline Solids. Aedermannsdorf, 1977; pp 465–470.

(14) Varughese, B.; Lee, Y.-K.; Tomozawa, M. Effect of Fictive Temperature on Mechanical Strength of Soda-lime Glasses. *J. Non-Cryst. Solids* **1998**, *241*, 134–139.

(15) Jain, V.; Varshneya, A. Finite-Element Analysis of Network Dilatation in Ion-Exchanged Glass Rods After Slicing. *J. Am. Ceram. Soc.* **1987**, *70*, 2–5.

(16) Tandia, A.; Vargheese, K. D.; Mauro, J. C.; Varshneya, A. K. Atomistic Understanding of Network Dilation Anomaly in Ion-exchanged Glass. *J. Non-Cryst. Solids* **2012**, *358*, 316–320.

(17) Kreski, P. K.; Varshneya, A. K.; Cormack, A. N. Investigation of Ion-exchanged 'Stuffed' Glass Structures by MD. *J. Non-Cryst. Solids* **2012**, *358*, 3539–3545.

(18) Fu, A. I.; Mauro, J. C. Mutual Diffusivity, Network Dilation, and Salt Bath Poisoning Effects in Ion-exchanged Glass. *J. Non-Cryst. Solids* **2013**, *363*, 199–204.

(19) Cooper, A.; Krohn, D. Strengthening of Glass Fibers II: Ion Exchange. *J. Am. Ceram. Soc.* **1969**, *52*, 665–669.

(20) Tandia, A.; Vargheese, K. D.; Mauro, J. C. Elasticity of Ion Stuffing in Chemically Strengthened Glass. *J. Non-Cryst. Solids* **2012**, *358*, 1569–1574.

(21) Tyagi, V.; Varshneya, A. K. Measurement of Progressive Stress Buildup During Ion Exchange in Alkali Aluminosilicate Glass. *J. Non-Cryst. Solids* **1998**, *238*, 186–192.

(22) Vargheese, K. D.; Tandia, A.; Mauro, J. C. Molecular Dynamics Simulations of Ion-exchanged Glass. *J. Non-Cryst. Solids* **2014**, *403*, 107–112.

(23) Brawer, S. A.; White, W. B. Raman Spectroscopic Investigation of the Structure of Silicate Glasses. I. The Binary Akali Silicates. *J. Chem. Phys.* **1975**, *63*, 2421–2432.

(24) McMillan, P. Structural Studies of Silicate Glasses and Melts–Applications and Limitations of Raman Spectroscopy. *Am. Miner.* **1984**, *69*, 622–644.

(25) Matson, D. W.; Sharma, S. K.; Philpotts, J. A. The Structure of High-silica Alkali-silicate Glasses. A Raman Spectroscopic Investigation. *J. Non-Cryst. Solids* **1983**, *58*.

(26) Furukawa, T.; Fox, K. E.; White, W. B. Raman Spectroscopic Investigation of the Structure of Silicate Glasses. III. Raman Intensities and Structural Units in Sodium Silicate Glasses. *J. Chem. Phys.* **1981**, *75*, 3226.

(27) Mysen, B. O.; Virgo, D.; Seifert, F. A. The Structure of Silicate Melts: Implications for Chemical and Physical Properties of Natural Magma. *Rev. Geophys.* **1982**, *20*, 353.

(28) Houde-Walter, S. N.; Inman, J. M.; Dent, A. J.; Greaves, G. N. Sodium and Silver Environments and Ion-Exchange Processes in Silicate and Aluminosilicate Glasses. *J. Phys. Chem.* **1993**, *97*, 9330–9336.

(29) Quaranta, A.; Rahman, A.; Mariotto, G.; Maurizio, C.; Trave, E.; Gonella, F.; Cattaruzza, E.; Gibaudo, E.; Broquin, J. E. Spectroscopic Investigation of Structural Rearrangements in Silver Ion-Exchanged Silicate Glasses. *J. Phys. Chem. C* **2012**, *116*, 3757–3764.

(30) Ingram, M.; Davidson, J.; Coats, A.; Kamitsos, E.; Kapoutsis, J. Origins of Anomalous Mixed-alkali Effects in Ion-exchanged Glasses. *Glastech. Ber. Glass Sci. Technol.* **2000**, *73*, 89–104.

(31) Varshneya, A. K. The Physics of Chemical Strengthening of Glass: Room for a New View. *J. Non-Cryst. Solids* **2010**, *356*, 2289–2294.

(32) Hale, D. K. Strengthening of Silicate Glasses by Ion Exchange. *Nature* **1968**, *217*, 1115–1118.

(33) Varshneya, A. Kinetics of Ion Exchange in Glass. *J. Non-Cryst. Solids* **1975**, *19*, 355–365.

(34) Garfinkel, H.; King, C. Ion Concentration and Stress in a Chemically Tempered Glass. *J. Am. Ceram. Soc.* **1970**, *53*, 686–691.

(35) Société des Produits Chimiques Harbonnières, *MSDS: Potassium Carbonate*; 2010; pp 1–7.

(36) Unuma, H.; Kokubo, T.; Sakka, S. Crystallization of Li-Si-ON Oxynitride Glasses. *J. Mater. Sci.* **1988**, *23*, 4399–4405.

(37) Novaes de Oliveira, A. P.; Barbieri, L.; Leonelli, C.; Manfredini, T.; Pellacani, G. C. Physical Properties of Quenched Glasses in the Li_2O-ZrO_2-SiO_2 System. *J. Am. Ceram. Soc.* **1996**, *79*, 1092–1094.

(38) Shelby, J.; Shelby, S. Phase Separation and the Properties of Lithium Calcium Silicate Glasses. *Phys. Chem. Glasses* **2000**, *41*, 59–64.

(39) Gee, I.; Holland, D.; McConville, C. Atomic Environments in Binary Lead Silicate and Ternary Alkali Lead Silicate Glasses. *Phys. Chem. Glasses* **2001**, *42*, 339–348.

(40) Hering, B.; Bliss, H. Diffusion in Ion Exchange Resins. *AIChE J.* **1963**, *9*, 495–503.

(41) Bliss, M.; Aker, P. M.; Windisch, C. F. Further Investigations of the Effect of Replacing Lithium by Sodium on Lithium Silicate Scintillating Glass Efficiency. *J. Non-Cryst. Solids* **2012**, *358*, 751–757.

(42) Mysen, B. O.; Finger, L. W.; Virgo, D.; Seifert, F. A. Curve-fitting of Raman Spectra of Silicate Glasses. *Am. Miner.* **1982**, *67*, 686–695.

(43) Xue, X.; Stebbins, J. F.; Kanzaki, M.; McMillan, P. F.; Poe, B. Pressure-induced Silicon Coordination and Tetrahedral Structural Changes in Alkali Oxide–Silica Melts up to 12 GPa: NMR, Raman, and Infrared Spectroscopy. *Am. Miner.* **1991**, *76*, 8–26.

(44) Long, D. A. *Raman Spectroscopy*; McGraw-Hill: New York, 1977.

(45) Potma, E. O.; Mukamel, S. In *Coherent Raman Scattering Microscopy*; Cheng, J.-X., Xie, X. S., Eds.; CRC Press, Taylor & Francis Group, 2013; pp 3–42.

(46) Zotov, N. Effects of Composition on the Vibrational Properties of Sodium Silicate Glasses. *J. Non-Cryst. Solids* **2001**, *287*, 231–236.

(47) Osipov, A.; Osipova, L. New Approach to Modeling of a Local Structure of Silicate Glasses and Melts. Journal of Physics: Conference Series. 2013; pp 12–19.

(48) Dietzel, A. Die Kationenfeldstärken und ihre Beziehungen zu Entglasungsvorgängen, zur Verbindungsbildung und zu den Schmelzpunkten von Silicaten. *Z. Electrochem.* **1942**, *48*, 9–23.

(49) Devine, R. A. B.; Dupree, R.; Farnan, I.; Capponi, J. J. Pressure-induced Bond-angle Variation in Amorphous SiO_2. *Phys. Rev. B* **1987**, *35*, 2560–2562.

(50) Newton, M.; Gibbs, G. *Ab initio* Calculated Geometries and Charge Distributions for H_4SiO_4 and $H_6Si_2O_7$ Compared with Experimental Values for Silicates and Siloxanes. *Phys. Chem. Miner.* **1980**, *6*, 221–246.

(51) Revesz, A.; Gibbs, G. In *The Physics of MOS insulators*; Lucovsky, G., Pantelides, S., Galeener, F., Eds.; Pergamon Press, Elsevier Inc.: London, UK, 1980.

(52) Williams, Q.; Hemley, R. J.; Kruger, M. B.; Jeanloz, R. High-pressure Infrared Spectra of α-Quartz, Coesite, Stishovite and Silica Glass. *J. Geophys. Res* **1993**, *98*, 22157–22170.

(53) Kihara, K.; Hirose, T.; Shinoda, K. Raman Spectra, Normal Modes and Disorder in Monoclinic Tridymite and its Higher Temperature Orthorhombic Modification. *J. Miner. Petrol. Sci.* **2005**, *100*, 91–103.

(54) McDonald, W. S.; Cruickshank, D. W. J. A Reinvestigation of the Structure of Sodium Metasilicate, Na_2SiO_3. *Acta Crystallogr.* **1967**, *22*, 37–43.

(55) Liu, F.; Garofalini, S. H.; King-Smith, R. D.; Vanderbilt, D. Structural and Electronic Properties of Sodium Metasilicate. *Chem. Phys. Lett.* **1993**, *215*, 401–404.

(56) Richet, P. Melting and Premelting of Silicates: Raman Spectroscopy and X-ray Diffraction of Li_2SiO_3 and Na_2SiO_3. *Phys. Chem. Miner.* **1996**, 157–172.

(57) Seemann, H. Die Kristallstruktur des Lithiummetasilikates, $(Li_2SiO_3)_x$. *Acta. Cryst.* **1956**, *9*, 251–252.

(58) Voellenkle, H. Verfeinerung der Kristallstrukturen von Li_2SiO_3 und Li_2GeO_3. *Z. Kristallogr.* **1981**, *154*, 77–81.

(59) Hesse, K. F. Refinement of the Crystal Structure of Lithium Polysilicate. *Acta. Cryst. B* **1977**, *33*, 901–902.

(60) Fuss, T.; Moguš-Milanković, A.; Ray, C. S.; Lesher, C. E.; Youngman, R.; Day, D. E. *Ex situ* XRD, TEM, IR, Raman and NMR Spectroscopy of Crystallization of Lithium Disilicate Glass at High Pressure. *J. Non-Cryst. Solids* **2006**, *352*, 4101–4111.

(61) de Jong, B.; Super, H.; Spek, A.; Veldman, N.; Nachtegaal, G.; Fischer, J. Structure and ^{29}Si MAS NMR of $Li_2Si_2O_5$ and $Ki_2Si_2O_5$. *Acta. Cryst. B* **1998**, *54*, 568–577.

(62) Pant, A. K.; Cruickshank, D. W. J. The Crystal Structure of α-$Na_2Si_2O_5$. *Acta. Cryst. B* **1968**, *24*, 13–19.

(63) You, J.; Jiang, G.-C.; Xu, K.-D. High Temperature Raman Spectra of Sodium Disilicate Crystal, Glass and its Liquid. *J. Non-Cryst. Solids* **2001**, *282*, 125–131.

(64) Smith, R. I.; West, A. R.; Abrahams, I.; Bruce, P. G. Rietveld Structure Refinement of Metastable Lithium Disilicate using Synchrotron X-ray Powder Diffraction Data from the Daresbury SRS 8.3 Diffractometer. *Powder Diffr.* **1990**, *5*, 137–143.

(65) Smith, R. I.; Howie, R. A.; West, A. R.; Aragon Pina, A.; Villafuerte Castrejon, M. E. The Structure of Metastable Lithium Disilicate, $Li_2Si_2O_5$. *Act. Cryst. C* **1990**, *46*, 363–365.

(66) Araki, T.; Zoltai, T. Refinement of a Coesite Structure. *Z. Kristallogr.* **1969**, *129*, 381–387.

(67) Levien, L.; Prewitt, C. High-pressure Crystal Structure and Compressibility of Coesite. *Am. Miner.* **1981**, *66*, 324–333.

(68) Hemley, R. Pressure dependence of Raman spectra of SiO_2 polymorphs α-quartz, coesite and stishovite. *High Pressure Research in Mineral Physics, Geophys. Monogr. Ser.* **1987**, *39*, 347–359.

(69) Sharma, S. K.; Mammone, J. F.; Nicol, M. F. Raman Investigation of Ring Configurations in Vitreous Silica. *Nature* **1981**, *292*, 140–141.

(70) Gillet, P.; Le Cléac'h, A.; Madon, M. High-temperature Raman Spectroscopy of SiO_2 and GeO_2 Polymorphs: Anharmonicity and Thermodynamic Properties at High Temperatures. *J. Geophys. Res* **1990**, *95*, 21635–21655.

(71) Norby, P. Synchrotron Powder Diffraction using Imaging Plates: Crystal Structure Determination and Rietveld Refinement. *J. Appl. Crystallogr.* **1997**, *30*, 21–30.

(72) Wright, A. F.; Lehmann, M. S. The Structure of Quartz at 25 and 590°C Determined by Neutron Diffraction. *J. Solid State Chem.* **1981**, *36*, 371–380.

(73) Hanic, F.; Sumichrast, L. α-β Phase Transition in Quartz. *Ceram. Silik.* **1974**, *18*, 1–9.

(74) D'Amour, H.; Denner, W.; Schulz, H. Structure Determination of α-Quartz up to 68×10^8 Pa. *Acta. Cryst. B* **1979**, *35*, 550–555.

(75) Dusek, M.; Petricek, V.; Wunschel, M.; Dinnebier, R. E.; van Smaalen, S. Refinement of Modulated Structures against X-ray Powder Diffraction Data with JANA2000. *J. Appl. Crystallogr.* **2001**, *34*, 398–404.

(76) Gualtieri, A. F. Accuracy of XRPD QPA using the Combined Rietveld-RIR Method. *J. Appl. Crystallogr.* **2000**, *33*, 267–278.

(77) Glinnemann, J.; King Jr., H. E.; Schulz, H.; Hahn, T.; la Placa, S.; Dacol, F. Crystal Structures of the Low-temperature Quartz-type Phases of SiO_2 and GeO_2 at Elevated Pressure. *Z. Kristallogr.* **1992**, *198*, 177–212.

(78) Hazen, R. M.; Finger, L. W.; Hemley, R. J.; Mao, H. K. High-pressure Crystal Chemistry and Amorphization of α-quartz. *Solid State Commun.* **1989**, *72*, 507–511.

(79) Ogata, K.; Takeuchi, Y.; Kudoh, Y. Structure of α-Quartz as a Function of Temperature and Pressure. *Z. Kristallogr.* **1987**, *179*, 403–413.

(80) Scott, J. F.; Porto, S. Longitudinal and Transverse Optical Lattice Vibrations in Quartz. *Phys. Rev.* **1967**, *161*, 903.

(81) Bates, J. B.; Quist, A. Polarized Raman Spectra of β-quartz. *J. Chem. Phys.* **1972**, *56*, 1528.

(82) Shapiro, S. M.; O'Shea, D. C.; Cummins, H. Z. Raman Scattering Study of the α-β Phase Transition in Quartz. *Phys. Rev. Lett.* **1967**, *19*, 361–364.

(83) McMillan, P. F.; Wolf, G. H.; Lambert, P. A Raman Spectroscopic Study of Shocked Single Crystalline Quartz. *Phys. Chem. Miner.* **1992**, *19*, 71–79.

(84) Hemley, R. J.; Mao, H. K.; Chao, E. C. T. Raman Spectrum of Natural and Synthetic Stishovite. *Phys. Chem. Miner.* **1986**, *13*, 285–290.

(85) Zotov, N.; Ebbsjö, I.; Timpel, D.; Keppler, H. Calculation of Raman Spectra and Vibrational Properties of silicate Glasses: Comparison between $Na_2Si_4O_9$ and SiO_2 Glasses. *Phys. Rev. B* **1999**, *60*, 6383–6397.

(86) Etchepare, J. Vibrational Normal Modes of SiO_2. I. α- and β-Quartz. *J. Chem. Phys.* **1974**, *60*, 1873.

(87) Dollase, W. A. Reinvestigation of the Structure of Low Cristobalite. *Z. Kristallogr.* **1965**, *121*, 369–377.

(88) Downs, R.; DC, P. The Pressure Behavior of α-Cristobalite. *Am. Miner.* **1994**, *79*, 9–14.

(89) Bates, J. B. Raman Spectra of α- and β-cristobalite. *J. Chem. Phys.* **1972**, *57*, 4042–4047.

(90) Palmer, D. C.; Russell, J.; Prewitt, C. T. Raman Spectroscopic Study of High-pressure Phase Transitions in Cristobalite. *Phys. Chem. Miner.* **1994**, *21*, 481–488.

(91) Swainson, I. P.; Dove, M. T.; Palmer, D. C. Infrared and Raman Spectroscopy Studies of the α–β Phase Transition in Cristobalite. *Phys. Chem. Miner.* **2003**, *30*, 353–365.

(92) Etchepare, J.; Merian, M.; Kaplan, P. Vibrational Normal Modes of SiO_2. II. Cristobalite and Tridymite. *J. Chem. Phys.* **1978**, *68*, 1531.

(93) Wyckoff, R. W. G. Crystal Structure of High Temperature Cristobalite. *Am. J. Sci.* **1925**, *9*, 448–459.

(94) Peacor, D. High-temperature Single-crystal Study of the Cristobalite Inversion. *Z. Kristallogr.* **1973**, *138*, 274–298.

(95) Baur, W. H. Silicon-oxygen Bond Lengths, Bridging Angles Si-O-Si and Synthetic Low Tridymite. *Acta. Cryst. B* **1977**, *33*, 2615–2619.

(96) Hirose, T.; Kihara, K.; Okuno, M.; Fujinami, S.; Shinoda, K. X-ray, DTA and Raman Studies of Monoclinic Tridymite and its Higher Temperature Orthorhombic Modification with Varying Temperature. *J. Miner. Petrol. Sci.* **2005**, *100*, 55–69.

(97) Kihara, K.; Hirose, T.; Shinoda, K. Raman Spectra, Normal Modes and Disorder in Monoclinic Tridymite and its Higher Temperature Orthorhombic Modification. *J. Miner. Petrol. Sci.* **2005**, *100*, 91–103.

(98) Wyckoff, R. W. G. XXIX. Kriterien für hexagonale Raumgruppen und die Kristallstruktur von β-Quarz. *Z. Kristallogr.* **1926**, *63*, 507–537.

(99) Tucker, M. G.; Keen, D. A.; Dove, M. T. A Detailed Structural Characterization of Quartz on Heating Through the α-β Transition. *Mineral. Mag.* **2001**, *65*, 489–507.

(100) Kihara, K. An X-ray Study of the Temperature Dependence of the Quartz Structure. *Eur. J. Mineral.* **1990**, *2*, 63–77.

(101) Graetsch, H.; Topalović-Dierdorf, I. ^{29}Si MAS NMR Spectrum and Superstructure of Modulated Tridymite L3-T_O(MX-1). *Eur. J. Mineral.* **1996**, *8*, 103–113.

(102) Boyer, H.; Smith, D. C.; Chopin, C.; Lasnier, B. Raman Microprobe (RMP) Determinations of Natural and Synthetic Coesite. *Phys. Chem. Miner.* **1985**, *12*, 45–48.

(103) Sato, M. X-ray Study of Tridymite. *Mineral. J. (Japan)* **1964**, *4*, 115–130.

(104) Galeener, F. A Model for the Distribution of Dihedral Angles in SiO_2-like Glasses. *J. Non-Cryst. Solids* **1985**, *75*, 399–405.

(105) Hill, R. J.; Gibbs, G. V. Variation in $d(T\text{-O})$, $d(T\cdots T)$ and $\angle TOT$ in Silica and Silicate Minerals, Phosphates and Aluminates. *Acta Crystallogr. Sect. B-Struc. Sci.* **1979**, *35*, 25–30.

(106) Birtch, E.; Mesko, M.; Shelby, J. Phase Separation and Properties of Lithium Barium Silicate Glasses. *Phys. Chem. Glasses* **2003**, *44*, 319–324.

(107) Tickle, R. Electrical Conductance of Molten Alkali Silicates. 2. Theoretical Discussion. *Phys. Chem. Glasses* **1967**, *8*, 113.

(108) Ledbetter, H.; Kim, S.; Balzar, D. Elastic Properties of Mullite. *J. Am. Ceram. Soc.* **1998**, *28*, 1025–1028.

(109) Schilling, F.; Hauser, M.; Sinogeikin, S.; Bass, J. Compositional Dependence of Elastic Properties and Density of Glasses in the System Anorthite-Diopside-Forsterite. *Contrib. Mineral. Petrol.* **2001**, *141*, 297–306.

(110) Mazurin, O. *Handbook of Glass Data*; Elsevier Science Ltd: Amsterdam, Netherlands, 1987; Vol. 00C; p 699.

(111) Mauro, J. C.; Loucks, R. J. Forbidden Glasses and the Failure of Fictive Temperature. *J. Non-Cryst. Solids* **2009**, *355*, 676–680.

Graphical TOC Entry

Mechanical-Structural Investigation of Ion-Exchanged Lithium Silicate Glass using Micro-Raman Spectroscopy

Courtney Calahoo, Ian S. Butler and J. W. Zwanziger